ASSESSMENT OF DIFFERENT FINITE ELEMENT MODELING TECHNIQUES ON DELAMINATION GROWTH IN ADVANCED COMPOSITE STRUCTURES

A THESIS SUBMITTED TO
THE GRADUATE SCHOOL OF NATURAL AND APPLIED SCIENCES
OF
MIDDLE EAST TECHNICAL UNIVERSITY

BY

İBRAHİM UÇAK

IN PARTIAL FULFILLMENT OF THE REQUIREMENTS
FOR
THE DEGREE OF MASTER OF SCIENCE
IN
MECHANICAL ENGINEERING

FEBRUARY 2012

Approval of the thesis:

ASSESSMENT OF DIFFERENT FINITE ELEMENT MODELING TECHNIQUES ON DELAMINATION GROWTH IN ADVANCED COMPOSITE STRUCTURES

submitted by **İBRAHİM UÇAK** in partial fulfillment of the requirements for the degree of **Master of Science in Mechanical Engineering Department, Middle East Technical University** by,

Prof. Dr. Canan Özgen
Dean, Graduate School of **Natural and Applied Sciences** _______________

Prof. Dr. Süha Oral
Head of Department, **Mechanical Engineering** _______________

Prof. Dr. K. Levend Parnas
Supervisor, **Mechanical Engineering Dept., METU** _______________

Examining Committee Members:

Prof. Dr. Bülent Doyum
Mechanical Engineering Department, METU _______________

Prof. Dr. K. Levend Parnas
Mechanical Engineering Department, METU _______________

Assoc. Prof. Dr. Serkan Dağ
Mechanical Engineering Department, METU _______________

Dr. Ergin Tönük
Mechanical Engineering Department, METU _______________

Prof. Dr. Altan Kayran
Aerospace Engineering Department, METU _______________

Date: 10.02.2012

I hereby declare that all information in this document has been obtained and presented in accordance with academic rules and ethical conduct. I also declare that, as required by these rules and conduct, I have fully cited and referenced all material and results that are not original to this work.

Name, Last Name: İbrahim Uçak

Signature:

ABSTRACT

ASSESSMENT OF DIFFERENT FINITE ELEMENT
MODELING TECHNIQUES ON DELAMINATION GROWTH IN
ADVANCED COMPOSITE STRUCTURES

Uçak, İbrahim
M. Sc., Department of Mechanical Engineering
Supervisor: Prof. Dr. K. Levend Parnas
February 2012, 100 pages

Virtual crack closure technique (VCCT) is commonly used to analyze debonding/delamination onset and growth in fiber reinforced composite assemblies. VCCT is a computational fracture mechanics based approach, and is based on Irwin's crack closure integral.

In this study, the debonding/delamination onset and growth potential in a bonded fiber reinforced composite skin-flange assembly is investigated using the VCCT. A parametric finite element analyses is conducted. The finite element analyses results are compared with coupon level experimental results available in the literature. The effects of different finite element modeling techniques are investigated. The bonded flange-assembly is modeled with pure solid (3D) elements, plane stress (2D) shell elements and plane strain (2D) shell elements. In addition, mesh density, element order and geometric non-linearity parameters are investigated as well. The accuracy and performance of these different modeling techniques are assessed. Finally, effect of initial defect location on delamination growth potential is investigated. The results presented in this study are expected to provide an insight to practicing engineers in the aerospace industry.

Keywords: Fiber Reinforced Composite Plastics, Debonding, Delamination, Finite Element Model, Virtual Crack Closure Technique, Damage Tolerance

ÖZ

KOMPOZİT YAPILARDA DELAMİNASYON İLERLEMESİNİN DEĞİŞİK SONLU ELEMAN MODELLEME TEKNİKLERİ İLE DEĞERLENDİRİLMESİ

Uçak, İbrahim
Yüksek Lisans, Makina Mühendisliği Bölümü
Tez Yöneticisi: Prof. Dr. K. Levend Parnas
Şubat 2012, 100 sayfa

Sanal çatlak kapama tekniği, güçlendirilmiş dokulu kompozit montajlarında yapışma ayrışması/delaminasyon başlangıcı ve ilerlemesi analizlerinde yaygın olarak kullanılmaktadır. Sayısal kırılma mekaniğine dayalı bir yaklaşım olan sanal çatlak kapama tekniği; Irwin'in çatlak kapama integrali üzerine kuruludur.

Bu çalışmada sanal çatlak kapama tekniği kullanılarak, yapıştırma ile bağlanmış güçlendirilmiş dokulu kompozit kabuk-flanş montajının ayrışması/ delaminasyon başlangıcı ve ilerlemesi incelenmektedir. Parametrik sonlu elemanlar analizi gerçekleştirilmiş olup; sonlu elemanlar analiz sonuçları literatürde bulunan kupon seviye deney sonuçları ile karşılaştırılmıştır. Değişik sonlu eleman modelleme tekniklerinin etkileri araştırılmaktadır. Yapıştırma ile bağlanmış flanş montajı, saf katı (3D) elemanlar, düzlem gerilme (2D) kabuk elemanları ve düzlem gerinim (2D) kabuk elemanları kullanılarak modellenmiştir. Ek olarak, eleman ağı yoğunluğu, eleman derecesi ve geometrik doğrusalsızlık parametreleri de incelenmektedir. Bu değişik modelleme tekniklerinin tutarlılık ve performansları değerlendirilmiştir. Son olarak, üretim esnasında ortaya çıkabilecek ilk hata konumunun delaminasyon büyümesi potansiyeline etkileri araştırılmıştır. Bu çalışmada sunulacak sonuçların havacılık sektöründe çalışan mühendisler için derinlemesine bir bakış sağlaması beklenmektedir.

Anahtar Kelimeler: Güçlendirilmiş Dokulu Kompozit Plastikler, Yapışma Ayrışması, Delaminasyon, Sonlu Elemanlar Modeli, Sanal Çatlak Kapama Tekniği, Hasar Toleransı

ACKNOWLEDGMENTS

The author wishes to express his deepest gratitude to his supervisor Prof. Dr. Levend Parnas for their guidance, advice, criticism, encouragements and insight throughout the research.

The author would also like to thank to his brother Dr. Alper Uçak for his invaluable support, suggestions and comments.

Last but not least, I would like to thank to my wife, and my parents for their continual support.

TABLE OF CONTENTS

LIST OF TABLES

TABLES

LIST OF FIGURES

FIGURES

CHAPTER 1

INTRODUCTION

1.1 Introduction

Fiber reinforced composite plastics (FRP) are increasingly becoming popular, especially in the aerospace, marine, energy and automotive industries, where low weight, high stiffness and high strength are required. In addition to their low weight-to-high stiffness and strength ratio, FRP's are also easy to tailor and have good endurance in harsh environments.

In assemblies, components made of FRP may either be mechanically fastened or bonded together. A typical example is the connection between the spars and the skins in a composite wing box which is depicted in Figure 1-1 and Figure 1-2. When mechanical joining/fastening is used, special precautions have to be taken, since this method can create discontinuities in the fibers of the composite, which in turn could reduce the endurance of the component. Hence, bonding is preferred in the assembly of FRP components/structures, which is also the cost and weight effective method. Bonding is also advantageous in terms of electrical and/or thermal insulation or conductivity, corrosion, fatigue resistance and damping characteristics.

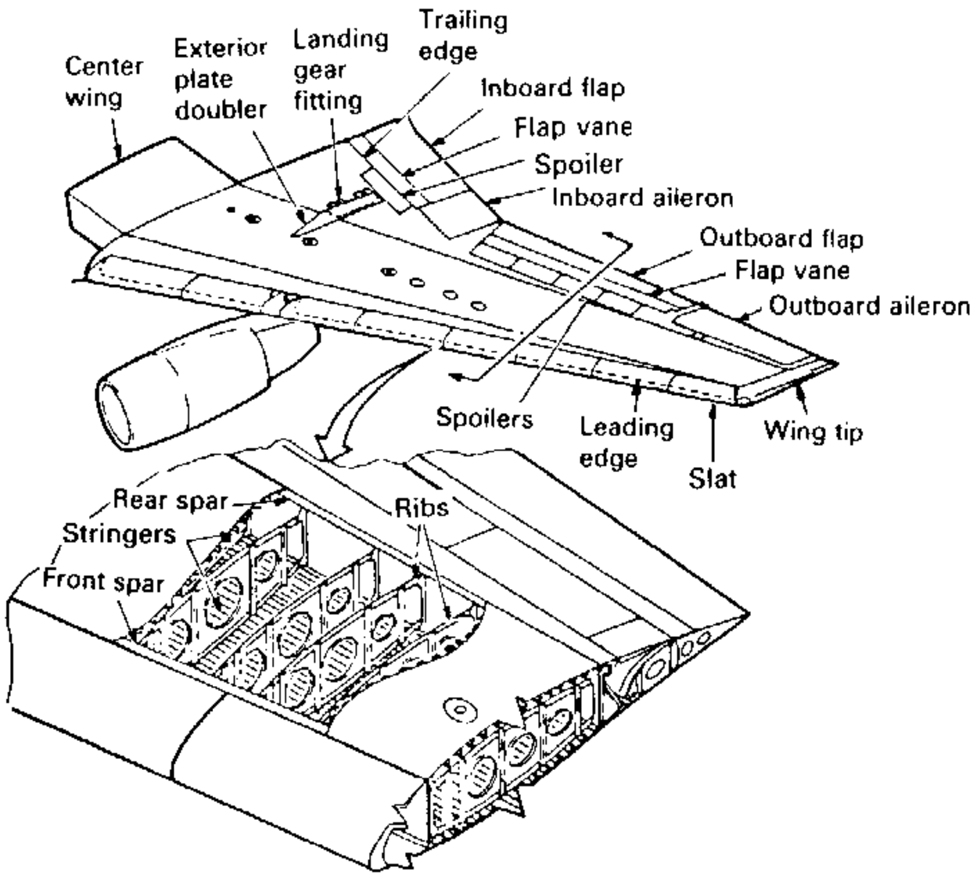

Figure 1-1: Wing box structure of an aircraft (Niu 2006)

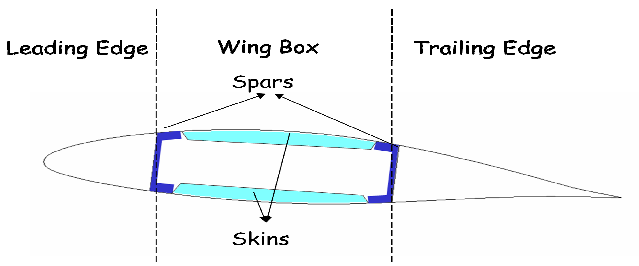

Figure 1-2: Schematic view of wing box

Several bonding methods are used in the industry, namely, co-bonding, co-curing, and secondary bonding. Since co-bonding and co-curing require special molds and special manufacturing requirements, secondary bonding is the simplest and preferred bonding technique. While bonding is preferred over mechanical joining, ensuring a quality of bonding has been a challenging task. In addition, bonded composite components are susceptible to debonding and delamination, which are the most common failure modes observed in composites (Pagano and Schoepner 2000). Hence, it is of particular interest to develop computational methods, which can predict the onset and growth of delamination. Modeling and prediction of delamination in composite materials is not a straight forward procedure, that is, the techniques and procedures that can be used to model and predict delamination have not been sufficiently implemented into commercially available computational or finite element tools.

In service, aerospace components mostly have small tolerable defects or flaws. These defects may have occurred due to in service conditions, or manufacturing errors. Hence, in the design process the effect of these tolerable defects or flaws should be accounted for to prevent catastrophic failures. This is called damage tolerant design. In the damage tolerant design, one of the techniques is using reduced allowable stress values in the design, which is a trade-off between weight and repair costs. The products are going to be heavier when an over-reduced allowable stress value is used, meaning more fuel consumption and low efficient vehicles. Products designed with an under-reduced allowable stress value could tolerate smaller damages, meaning more frequent in service repairs, more expensive repair and operating costs. On the other hand, if the effect of a particular flaw (on the delamination growth potential) could be determined using computational tools, a more sound and efficient design could be developed without compromising safety.

1.2 Scope of the Work and Objectives

In this study the debonding/delamination onset and growth in a bonded skin-flange assembly will be analyzed by means of detailed finite element analyses. The finite element analyses results will be compared with coupon level experimental results available in the literature. The effect of different finite element modeling techniques will be investigated. The bonded skin-flange assembly will be modeled with solid (3D) elements, plain stress shell (2D) elements and plain strain (2D) shell elements. The accuracy and performance of these different modeling techniques will be assessed. The effect of geometrically linear and non-linear analyses techniques, element order, and mesh density will be investigated. Furthermore the effect of initial defect location on delamination growth potential will be investigated. The results presented in this study are expected to provide important insight to practicing engineers in the aerospace industry.

1.3 Organization

Organization of this thesis is as follows:

Chapter 2 contains a brief survey of causes of delamination in composite components. Also explained are the experimental techniques that have been used to determine the fracture toughness of composite specimens, and computational techniques that can be used to predict the onset and growth of debonding/delamination in composite components.

Chapter 3 provides the description of experimental studies that have been used as benchmark verification cases to determine the accuracy of the finite element model, used in this study.

Chapter 4 presents a detailed explanation of the finite element model used in this study, and the results. After the details of the finite element models considered are explained, the global (force-deformation and force-strain) result obtained from the different finite element analyses are compared with the experimental ones. The results of the parametric study conducted to investigate the potential of delamination growth using a fracture mechanics based approach (VCCT) are given. Also provided are the details and results of the analyses conducted to investigate the effect of initial defect location on delamination growth potential.

Finally, Chapter 5 provides the conclusions and recommendations for future research.

CHAPTER 2

LITERATURE SURVEY

2.1 Introduction

Fiber reinforced composite plastics (FRP) are increasingly becoming popular, especially in aerospace, marine, energy and automotive industries, where low weight, high stiffness and high strength are required. In addition to their low weight to stiffness and strength ratio, FRP's are also easy to tailor, have good endurance in harsh environments and have superior fatigue properties compared to traditional materials.

Composite materials are composed of two or more materials, and have superior material properties compared to the properties of each individual material composing the composite. In general the two constituents used are the fiber and the matrix. Typically fibers provide the strength and stiffness. The matrix holds the fibers together, protects the fibers from external environment and transfers the load between the fibers. Fibers may be continuous in the form of unidirectional, woven or roving; or discontinuous as chopped or mat fibers as depicted in Figure 2-1. Typical fibers include glass, carbon and kevlar. Matrices could consist of polymers, ceramics and metals.

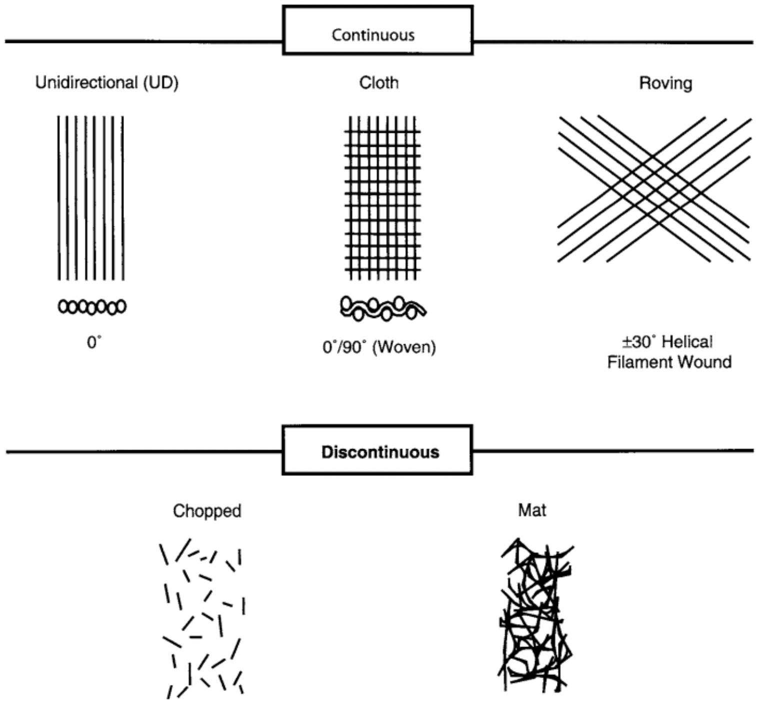

Figure 2-1: Typical fibers (Campbell 2004)

In modern aircrafts, decreasing the number of components in an assembly is the primary objective in order to reduce the assembly time and cost. Hence, ideally it is preferred that composite assemblies are cured together. However sometimes this may introduce very expensive and complex molds. In these situations, other assembly means such as mechanically fastening or bonding may be preferred. The advantages and disadvantages of mechanically fastening and bonding are summarized in Table 2-1. Mechanical fastening and bonding samples could be seen in Figure 2-2.

Table 2-1: Comparison of mechanically fastening to bonding

	Advantages	Disadvantages
Mechanically Fastening	• Easy inspection, • Easy repair, • Could be applied to any thickness, • Could be disassembled.	• Many parts in the assembly, • Stress concentration created, • Fatigue susceptible, • Additional sealing required, • Corrosion susceptible.
Bonding	• Few parts in the assembly, • Continuous load transfer, • Fatigue tolerant, • No additional sealing required, • Light-weight structure, • Smooth contour for aerodynamic surfaces, • Corrosion resistant, • No stress concentration created,	• Difficult inspection, • Surface preparation required, • Susceptible to environmental effects, • Limited thickness, • Could not be disassembled, • Small tension loadings could be transferred, • New design guidelines required.

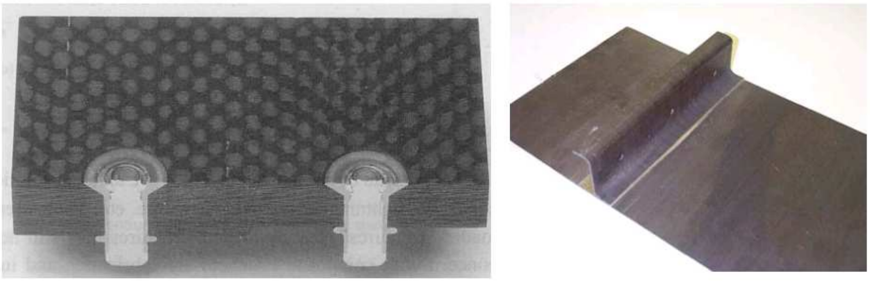

Figure 2-2 Mechanical fastening and bonding examples (Heslehurst 2008)

When mechanical joining/fastening is used, special precautions have to be taken, since this method creates discontinuities in the fibers of the composite, which in turn could reduce the endurance of the components and create stress concentrations. Hence, bonding may be preferred in the assembly of FRP components/structures, which is also the cost and weight effective method in most cases. There are several types of bonding, that is, co-curing, co-bonding or secondary bonding. From a structural point of view, co-curing is the strongest and secondary bonding is the weakest bonding type. However, co-curing requires extensive tooling and tight tolerances that makes it infeasible most of the time.

While bonding is preferred over mechanical joining, bonded composite components are susceptible to debonding and delamination, which are the most common failure modes observed in composites. Delamination is essentially the separation of the plies from each other, and can lead to component failure. Figure 2-3 depicts the different types of delamination modes observed in composite components. Delamination is usually caused due to structural defects or discontinuities, and usually is observed when the thickness of the component is changed (internal or external ply drop), at skin-stiffener connections or at stress-free edges.

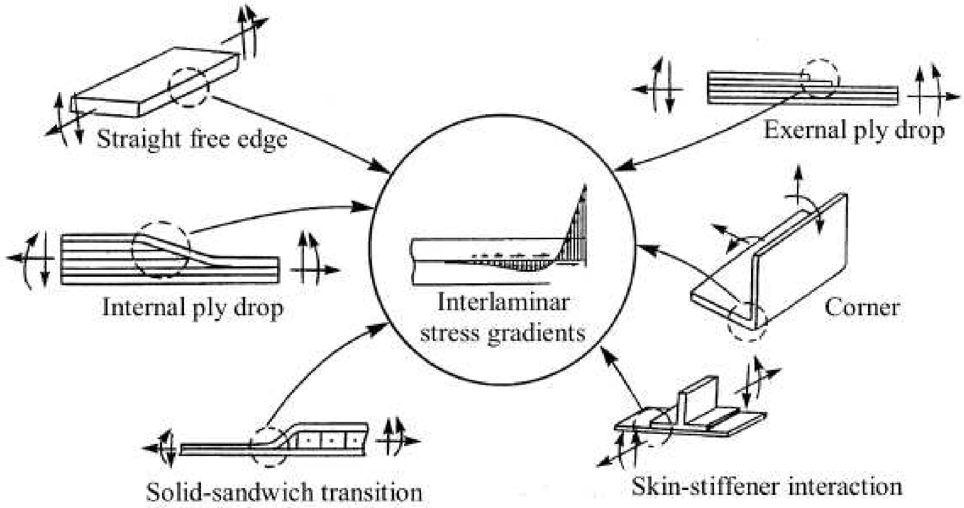

Figure 2-3: Sources of geometric and material discontinuities (Miracle and Donaldson 2001)

2.2 Causes of Delamination: A Fracture Mechanics Approach

Static or dynamic loads that have been applied to a composite component or structure will cause interlaminar shear and tension stresses. When the interlaminar strain energy release due to shear and tension stress gradients that occur at the discontinuities exceed a critical threshold called fracture toughness, delamination will initiate. Figure 2-4 depicts the commonly observed delamination fracture modes. As depicted in Figure 2-4, fracture modes can be divided into three types as:

- Mode I, or the opening mode, where crack faces move directly apart due to interlaminar tension;
- Mode II, or the sliding mode, where the crack surfaces slide over each other perpendicular to the crack tip due to interlaminar shear;

- Mode III, or the scissoring or tearing mode, where the crack surfaces slide over each other parallel to the crack tip due to interlaminar shear.

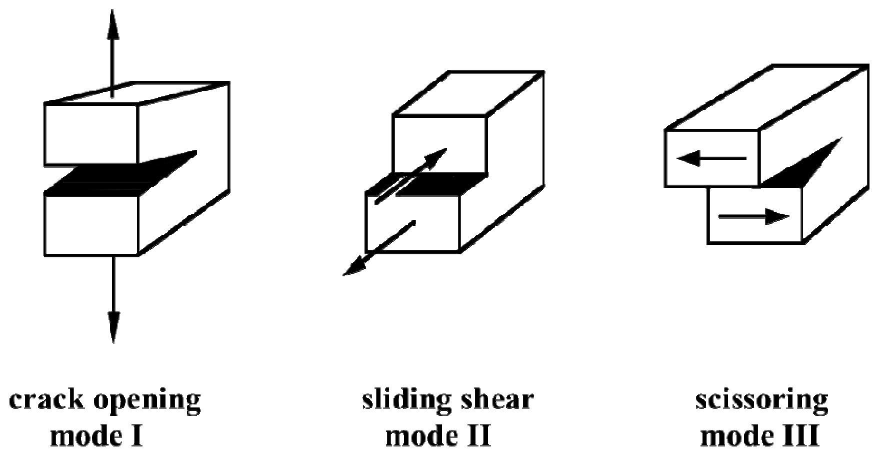

Figure 2-4: Common modes of delamination fracture (Krueger 2002)

In the fracture mechanics based approach; the computationally calculated strain energy release rate is compared with the experimentally evaluated critical value to determine the potential for delamination/crack growth. Experimental methods used to determine this critical value, the fracture toughness, are presented in Section 2.2.1. Several failure criteria are suggested by researchers which are described in detail by Reeder (2004).

The simplest criteria to determine the onset of delamination growth is based on solely mode I or mode II crack opening modes. The criterion based on pure mode I crack opening reads (Whitcomb 1986):

$$\frac{G_I}{G_{IC}} = 1 \qquad 2\text{-}1$$

where G_I is the analytically computed mode I strain energy release rate; and G_{IC} is the experimentally determined mode I fracture toughness of the material. Equation (2-1) simply indicates that there is a potential for delamination growth, when the computationally determined mode I strain energy release rate exceeds the mode I fracture toughness of the material. Similarly, Gillespie et al. (1985) proposed a criterion based on pure mode II crack opening:

$$\frac{G_{II}}{G_{IIC}} = 1 \qquad 2\text{-}2$$

where G_{II} and G_{IIC} are the analytically computed mode II strain energy release rate; and the experimentally determined mode II fracture toughness of the material respectively. Similarly Equation (2-2) indicates that delamination growth will occur when the computationally determined mode II strain energy release rate exceeds the mode II fracture toughness of the material.

While the delamination onset criteria presented in Equations (2-1) and (2-2) are very informative, engineering structures/components are subjected to complex loading conditions. Hence, delamination onset criteria based on mixed-mode strain energy release have been proposed. Wu and Reuter (1965) proposed a power law mixed-mode criterion in the form:

$$\left(\frac{G_I}{G_{IC}}\right)^{\alpha} + \left(\frac{G_{II}}{G_{IIC}}\right)^{\beta} = 1 \qquad 2\text{-}3$$

where α and β experimentally determined constants. Equation (2-3) has been frequently used in the literature and the constants α and β are determined by the method of least squares. Although Equation (2-3) is a non-linear function, when the exponents $\alpha = \beta = 1$, a linear criterion is obtained. Benzeggagh and Kenane (1996) proposed a mixed-mode fracture criterion in the form:

$$G_C = G_{IC} + (G_{IIC} - G_{IC})\left(\frac{G_{II}}{G_T}\right)^{\eta} \quad \text{2-4}$$

where G_T $(=G_1+G_2+G_3)$ is the total energy release rate; G_C is the interlaminar fracture toughness; and η is a constant. The constant η is determined by plotting G_{II}/G_T versus G_C as shown in Figure 2-5, and delamination is assumed to occur when $G_T/G_C>1$.

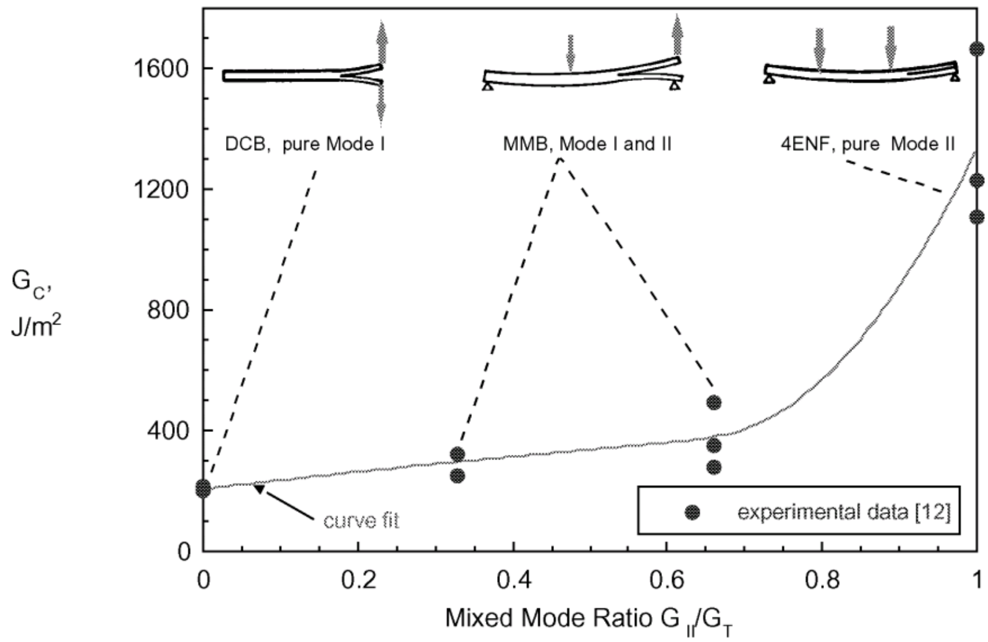

Figure 2-5: Mixed mode fracture criterion (Hansen and Martin 1999)

2.2.1 Experimental Procedures to Determine the Fracture Toughness

The fracture toughness is a material property independent from the geometry (Krueger 1994). Hence, the critical energy release rate of a specimen or the fracture toughness can be determined using simple experiments (O'Brien 1998). These tests include:

- Mode I test; Double cantilever beam (DCB) test to determine G_{IC} as per ASTM D5528 (2007);
- Mode II test; End Notched Flexure (ENF) test to determine G_{IIC} as per ASTM STP 1110 (1991);
- Mixed mode test; Mixed Mode Bending (MMB) or Single Leg Bending (SLB) tests to determine mode I and mode II interaction.

Double cantilever beam (DCB), end notched flexure (ENF), mixed mode bending (MMB), and single leg bending (SLB) test setups are depicted in Figure 2-6, Figure 2-7, Figure 2-8, and Figure 2-9 respectively.

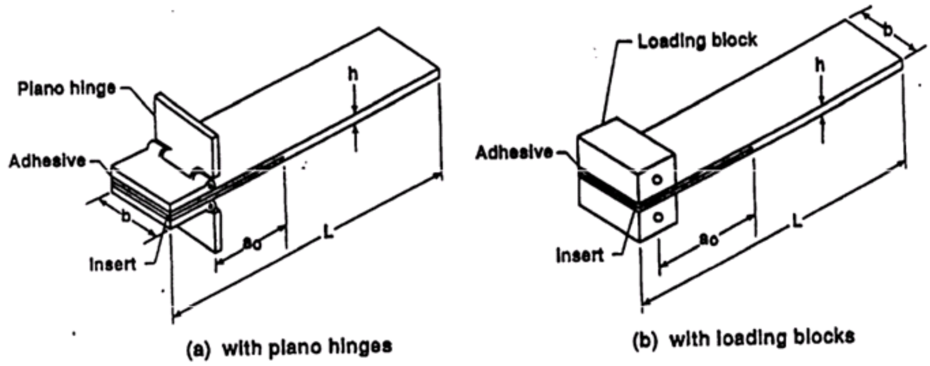

Figure 2-6: Double Cantilever Beam test setup (MIL-HDBK-17-1E 1997)

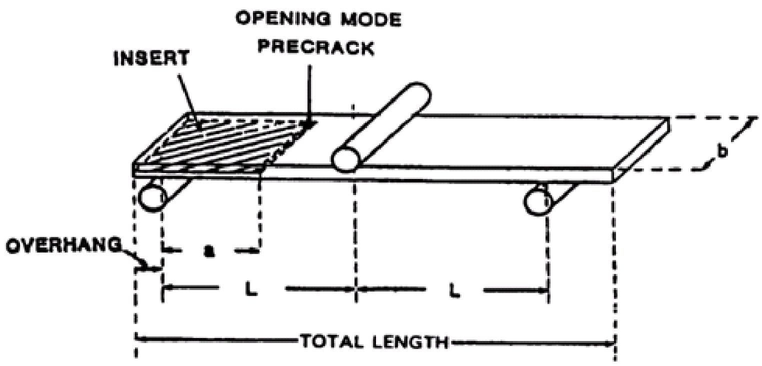

Figure 2-7: End Notched Flexure (ENF) test setup (MIL-HDBK-17-1E 1997)

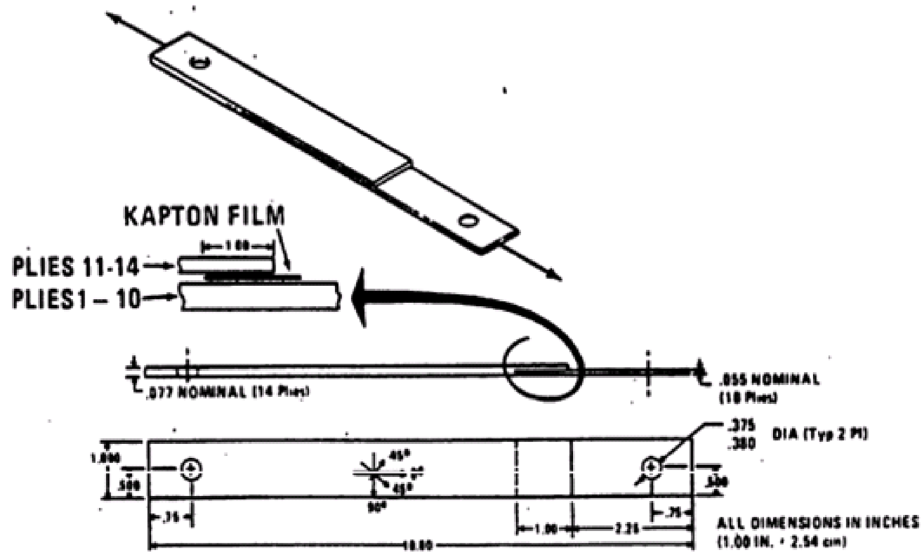

Figure 2-8: Mixed mode crack lap shear test setup (MIL-HDBK-17-1E 1997)

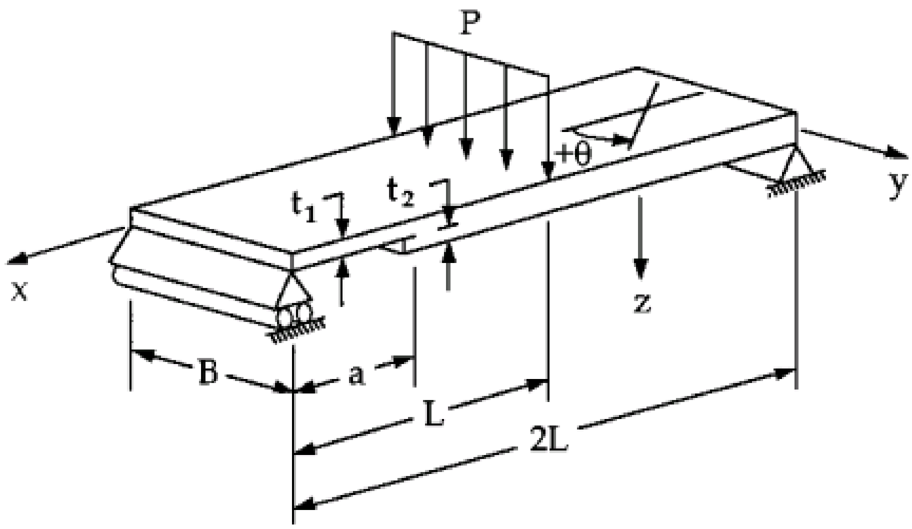

Figure 2-9: Single Leg Bending (SLB) test setup (MIL-HDBK-17-1E 1997)

2.3 Delamination Modeling and Prediction Background

With composite materials becoming more and more popular, it is of particular interest to develop computational methods, which can predict the onset and growth of delamination. Modeling and prediction of delamination in composite materials is not a straight forward procedure, that is, the techniques and procedures that can be used to model and predict delamination have not been sufficiently implemented into commercially available computational or finite element tools. Never the less, a number of researches successfully used computational mechanics based models to predict the onset and growth of delamination in composite structures. Mainly two computational methods exist; the cohesive zone modeling and the crack closure method based on computational fracture mechanics.

2.3.1 Cohesive Zone Modeling

Cohesive zone approach has been extensively used in the literature to simulate fracture in elastic-plastic solids such as rocks and concrete (Tvergaard and Hutchinson 1992), and interface debonding (Camanho et al. 2001, Camanho and Davila 2002, Wei and Hutchinson 1998).

In the cohesive zone approach the interphase between the two bonded materials are modeled using cohesive elements, and the mechanical response (stress-strain or force-deformation) of the cohesive elements are described using a constitutive model. The constitutive models used in the cohesive zone approach are based either on continuum mechanics or a traction-separation description at the interfaces. For modeling delamination initiation and growth in composite materials, generally a traction-separation based approach is used.

When cohesive elements are used to model delamination initiation and growth in composite materials, no assumptions has to be made of the initial flaw, debond or crack location, and the direction of the delamination propagation. However, in cohesive zone approach a very fine mesh has to be used in order to arrive at an accurate and stable result. It was shown by Alfano and Crisfield (2001), that the results produced by cohesive zone modeling are mesh sensitive and that care must be taken when using this approach.

2.3.2 Crack Closure Method

Two methods exist that are used to predict the onset and growth of delamination, and both are based on Irwin's crack closure integral:

- Crack closure or the two-step virtual crack closure method
- Virtual crack closure method

2.3.2.1 Crack Closure Method

The main idea behind the crack closure method, which is sometimes referred to as the two step virtual crack closure method (not to be confused with the virtual crack closure method) is that the energy dissipated when a crack grows by Δa is equal to the energy required to close the crack by Δa as presented in

Figure 2-10. As apparent from its name, this method requires two sets of analysis to determine the energy release for a given crack length. In this approach, a finite crack length is assumed *($a+\Delta a$)*. The first-step analysis is conducted with finite crack length a, to determine the tension and shear forces at the crack tip (Figure 2-10). Then, in the second-step analysis, the crack is extended to $a+\Delta a$ (or closed to $a-\Delta a$), and the normal and shear deformations at the crack opening are calculated. With reference to Figure 2-10, the two-step virtual crack closure method is based on the premises the energy released to extend the crack from point l to i, is equal to the energy required to close the crack between l and i (or vice-versa). Using basic thermodynamic principles, the work done during crack extension (or the work required to close the crack) and the energy release rate can be calculated respectively as:

$$\Delta E = \frac{1}{2}\left[X_{1l} \cdot \Delta u_{2l} + Z_{1i} \cdot \Delta w_{2l}\right] \qquad 2\text{-}5$$

$$G = \frac{\Delta E}{\Delta A} \qquad 2\text{-}6$$

In Equation (2-5) the subscripts *1* and *2* refer to the first step and second step analysis; the subscripts l and i denote the nodal coordinate; X and Z are the nodal forces; u and w are the nodal displacements (see also Figure 2-10); and ΔA is the crack surface area.

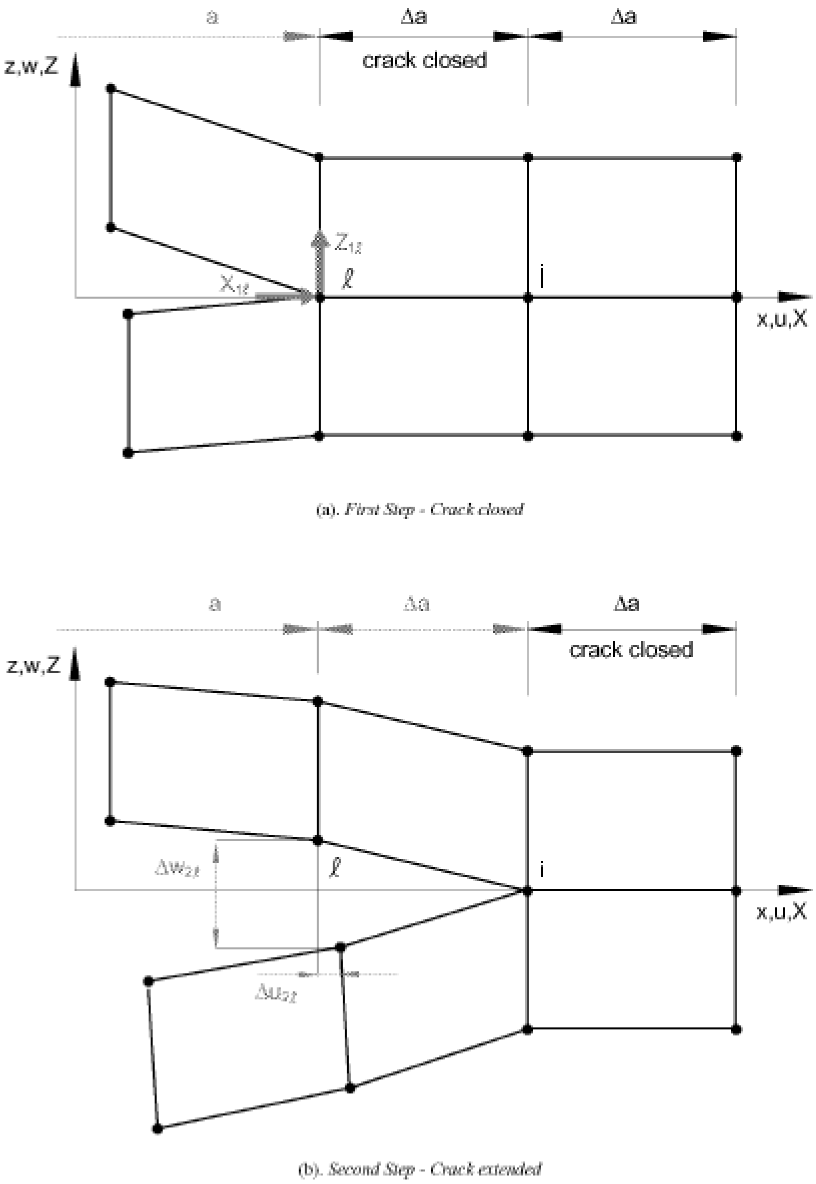

Figure 2-10: Schematic presentation of the two-step virtual crack closure method (Krueger 2002)

2.3.2.2 Virtual Crack Closure Method

The virtual crack closure method, which is also called the modified virtual crack closure method, is very similar to the two-step virtual crack closure method with the exception that it requires only one set of analysis to calculate the energy release rate for a given finite crack length. Numerous researchers have applied the VCCT to analyze the crack growth properties of an interlaminar damage in a range of structures, including fracture mechanics test specimens (Jimenez and Miravete 2004, Krueger 1994, Krueger et al. 1993); bonded joints (Johnson et al. 1998, Krueger et al. 2001, Yarrington and Collier 2006) and the behavior of edge delaminations (Whitcomb and Raju 1984).

The virtual crack closure method assumes that if the crack extension or closure length Δa is small enough, then the normal and shear deformations when the crack is extended from a to $a+\Delta a$ (or from l to i in Figure 2-10 and Figure 2-11) are approximately the same. Similar to the two-step virtual crack closure method, the virtual crack closure method is based on the premises the energy released to extend the crack from point l to i, is equal to the energy required to close the crack between l and i (or vice-versa). For the deformed geometry depicted in Figure 2-11, again using basic thermodynamic principles, the work done during crack extension (or the work required to close the crack) and the energy release rate can be calculated respectively as:

$$\Delta E = \frac{1}{2}\left[X_i \cdot \Delta u_l + Z_i \cdot \Delta w_l\right] \qquad \text{2-7}$$

$$G = \frac{\Delta E}{\Delta A} \qquad \text{2-8}$$

A comparison of Equation (2-7) with (2-5) shows that except the analysis step indices the equations are identical. However, due to its simplicity the virtual crack closure method is usually preferred in debonding/delamination analysis. A comparison of two-step virtual crack closure and virtual crack closure methods was conducted by Bonhomme et al. (2009).

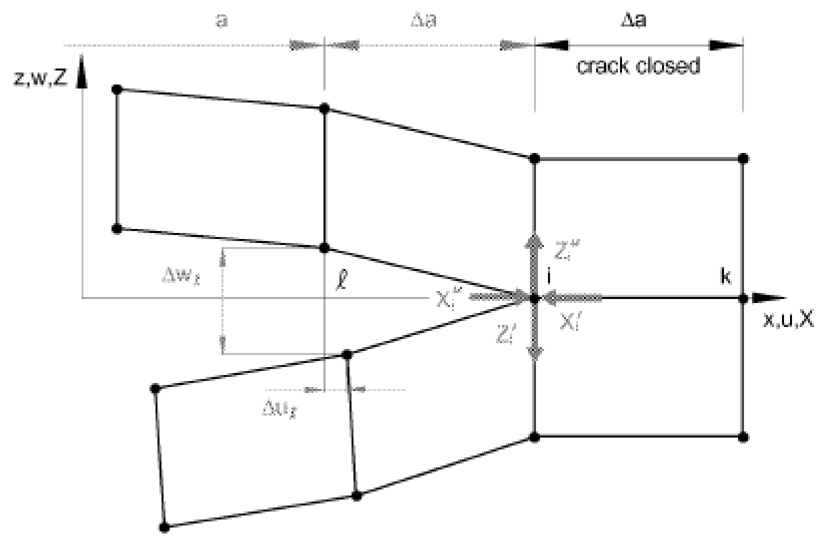

Figure 2-11: Schematic presentation of the virtual crack closure method (Krueger 2002)

2.4 Delamination Modeling and Prediction: The Crack Closure Method

The energy release rates presented in Equations (2-5) through (2-8) are generic, and in a computational fracture mechanics study they need to be modified depending on the type of elements used, that is, 2D or 3D elements with linear or quadratic formulations, and type of analysis conducted, i.e. linear and non-linear analysis. In this sub-section a brief summary of the different energy release rate formulation for different element and analysis types is presented. For more details the interested reader is referred to Krueger (2002).

2.4.1 Two Dimensional Models

In two-dimensional (2D) models the crack is modeled as a one-dimensional discontinuity. The 2D model can consist of shell elements or 3D plane stress/plane strain elements, as depicted in Figure 2-12. It must be noted that the term two-dimensional model does not relate to the element type used (2D or 3D), rather means that the crack is modeled as a line or one-dimensional discontinuity. Since the crack is model as a one-dimensional discontinuity, for these models the mode III energy release rate will be equal to zero, that is:

$$G_{III} = 0 \tag{2-9}$$

Using basic mechanics principles, for four noded linear elements the strain energy release rates for the remaining fracture modes can be written as:

$$G_I = -\frac{1}{2\Delta A} Z_i \left(w_l - w_{l*}\right) \tag{2-10}$$

$$G_{II} = -\frac{1}{2\Delta A} X_i \left(u_l - u_{l*}\right) \tag{2-11}$$

The total energy release rate becomes:

$$G_T = G_I + G_{II} + G_{III} \tag{2-12}$$

where ΔA is the crack surface area; X_i and Z_i are the shear and tension forces at the crack tip (node i) respectively; u_l and w_l are the relative sliding and opening displacements of the upper crack segment at node l respectively; and u_l^* and w_l^* are the relative displacements of the lower crack segment at node l as shown in Figure 2-12.

It must be noted that Equation 2-12 is valid for both linear and quadratic elements, and 2D and 3D models. For eight noded quadratic elements, the strain energy release rate equations are given by Raju (1987) as:

$$G_I = -\frac{1}{2\Delta A}\left[Z_i\left(w_l - w_{l*}\right) + Z_j\left(w_m - w_{m*}\right)\right] \qquad \text{2-13}$$

$$G_{II} = -\frac{1}{2\Delta A}\left[X_i\left(u_l - u_{l*}\right) + X_j\left(u_m - u_{m*}\right)\right] \qquad \text{2-14}$$

where X_i and Z_i are the shear and tension forces at the crack tip (node i) respectively; X_j and Z_j are the shear and tension forces at the mid-nodes (node j) respectively; u_l and w_l are the relative displacements of the upper crack segment at node l; u_l^* and w_l^* are the relative displacements of the lower crack segment at node l; u_m, w_m and u_m^*, w_m^* are the displacements of the mid-node behind the crack tip as shown in Figure 2-12.

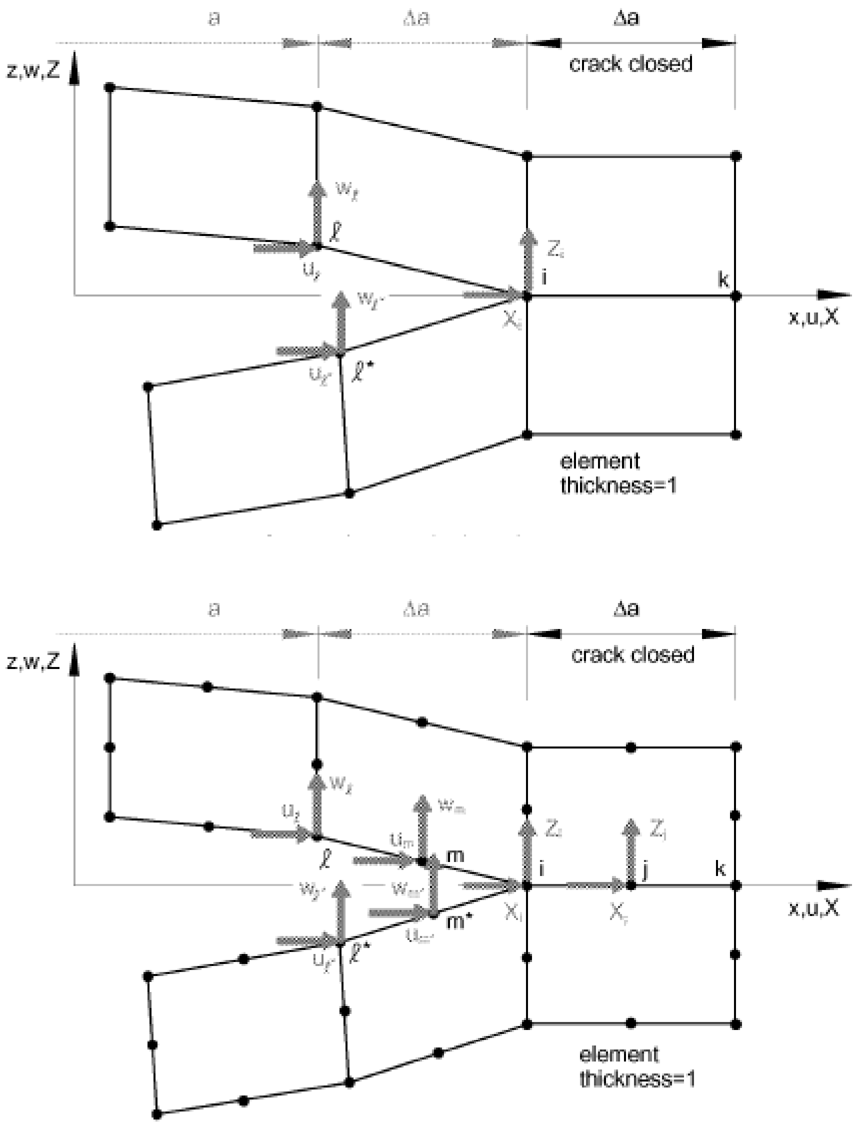

Figure 2-12: Two-dimensional virtual crack closure method for linear and quadratic elements (Krueger 2002)

2.4.2 Three Dimensional Models

In three-dimensional (3D) models the crack is modeled as a two-dimensional discontinuity with a surface area. These models may consist of shell elements or 3D brick elements, as depicted in Figure 2-13.

For eight-noded (linear) solid elements, strain energy release rates can be written as;

$$G_I = -\frac{1}{2\Delta A} Z_{Li}\left(w_{Ll} - w_{Ll*}\right) \tag{2-15}$$

$$G_{II} = -\frac{1}{2\Delta A} X_{Li}\left(u_{Ll} - u_{Ll*}\right) \tag{2-16}$$

$$G_{III} = -\frac{1}{2\Delta A} Y_{Li}\left(v_{Ll} - v_{Ll*}\right) \tag{2-17}$$

where X_{Li} , Y_{Li} and Z_{Li} are forces at column L, row I; u_{Li} , w_{Li} and v_{Li} are the relative displacements of the upper crack segment at behind the crack; and u_{Li}^{*} , w_{Li}^{*} and v_{Li}^{*} are the relative displacements of the lower crack segment behind the crack as shown in Figure 2-13.

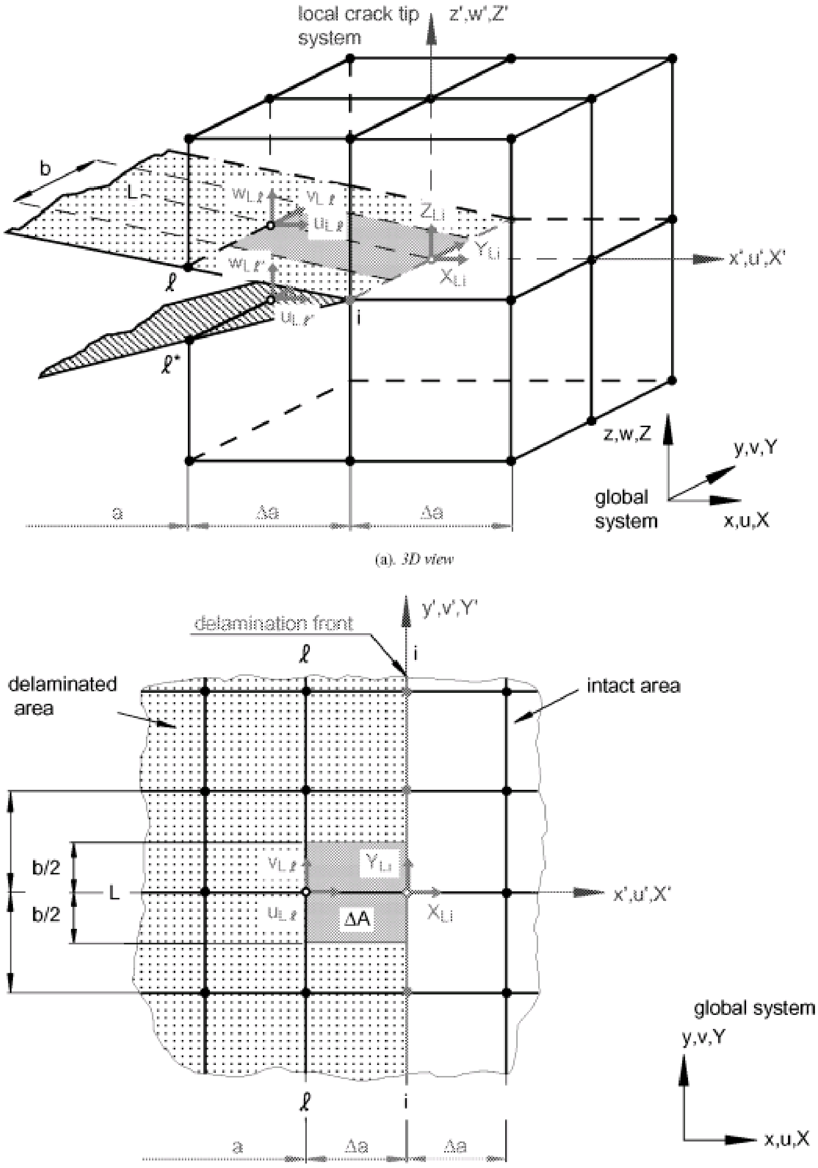

Figure 2-13: Three-dimensional virtual crack closure method for linear elements (Krueger 2002)

For twenty-noded (quadratic) solid elements, strain energy release rates can be written as;

$$G_I = -\frac{1}{2\Delta A}\left[\frac{1}{2}Z_{Ki}(w_{Kl} - w_{Kl^*}) + Z_{Li}(w_{Ll} - w_{Ll^*}) + Z_{Lj}(w_{Lm} - w_{Lm^*}) + \frac{1}{2}Z_{Mi}(w_{Ml} - w_{Ml^*})\right] \qquad \text{2-18}$$

$$G_{II} = -\frac{1}{2\Delta A}\left[\frac{1}{2}X_{Ki}(u_{Kl} - u_{Kl^*}) + X_{Li}(u_{Ll} - u_{Ll^*}) + X_{Lj}(u_{Lm} - u_{Lm^*}) + \frac{1}{2}X_{Mi}(u_{Ml} - u_{Ml^*})\right] \qquad \text{2-19}$$

$$G_{III} = -\frac{1}{2\Delta A}\left[\frac{1}{2}Y_{Ki}(v_{Kl} - v_{Kl^*}) + Y_{Li}(v_{Ll} - v_{Ll^*}) + Y_{Lj}(v_{Lm} - v_{Lm^*}) + \frac{1}{2}Y_{Mi}(v_{Ml} - v_{Ml^*})\right] \qquad \text{2-20}$$

where X_{Ki} , Y_{Ki} and Z_{Ki} are forces at column *K*, row *i*; u_{Ki} , w_{Ki} and v_{Ki} are the relative displacements of the upper crack segment at column *K*, row *i* behind the crack; and u_{Ki}^* , w_{Ki}^* and v_{Ki}^* are the relative displacements of the lower crack segment behind the crack at column *K*, row *i* as shown in Figure 2-14.

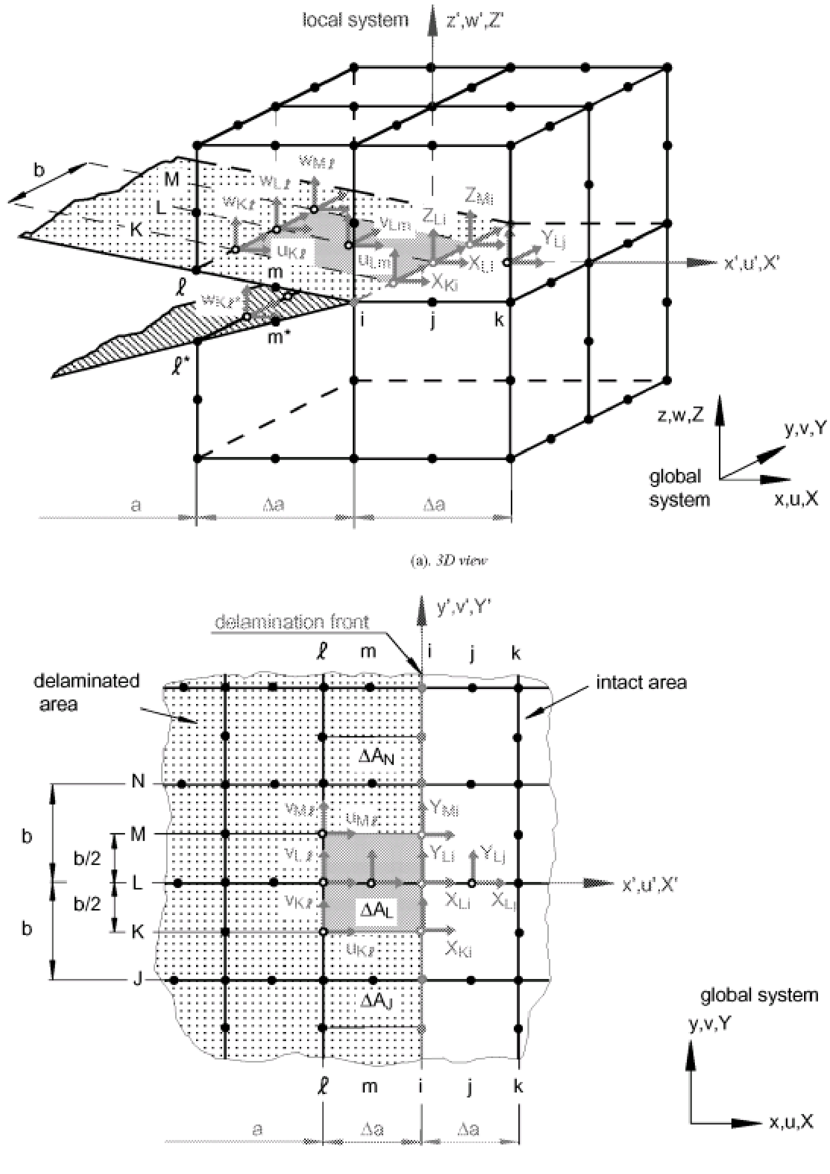

(b). *Top view of upper surface (lower surface terms are omitted for clarity)*

Figure 2-14: Three-dimensional virtual crack closure method for quadratic elements (Krueger 2002)

2.4.3 Further Modeling Considerations

The equations presented in Sections 2.4.1 and 2.4.2 are valid for geometrically linear analyses, assume that the element length in front and behind the crack are the same, and further assume that for 3D models the element widths along the delamination are the same.

In case of a geometrically non-linear analysis where large deformations occur, a coordinate transformation should be done prior to calculation of strain energy release rates. This transformation is depicted in Figure 2-15.

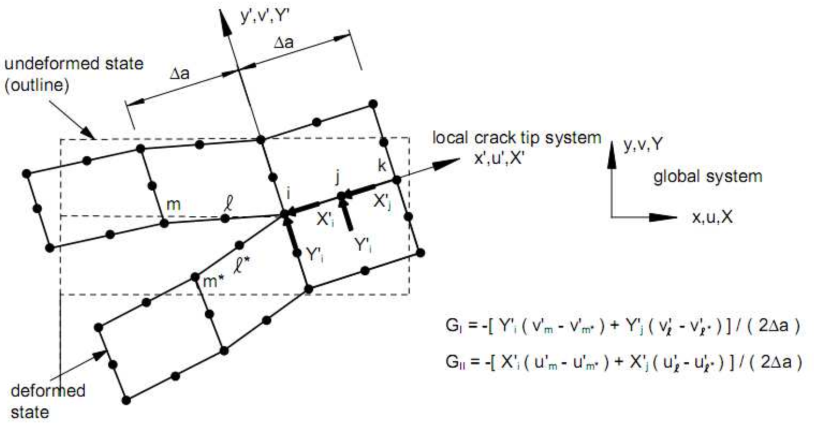

Figure 2-15: Local crack tip coordinate system (Krueger and Cvitkovich 1999)

It must be noted that only geometrical nonlinearities are considered in this study, and material nonlinearities are ignored. Hence, all the deformations reported in this study are elastic deformations. As a consequence, the total strain energy release rates calculated in this study are equal to the elastic strain rates. The strain release rate formulations presented in this chapter are valid for both geometrical linear and nonlinear analyses as long as coordinate transformation is conducted as described in the previous paragraph. It must also be noted that this statement may not be true for material nonlinearities where additive decomposition of the total strain into elastic and plastic parts is assumed (Kohnle et al. 2002).

CHAPTER 3

DESCRIPTION OF BENCHMARK EXAMPLES

3.1 Introduction

In an attempt to investigate skin-stiffener debonding in fiber reinforced composite components, a comprehensive experimental study was conducted by Kruger and Cvitkovich (1999). Some of the specimens tested by Kruger and Cvitkovich (1999) are chosen as benchmark verification examples, and used to verify the accuracy of the finite element model used in this study. In this chapter, a brief summary of the experimental study conducted by Kruger and Cvitkovich (1999) will be presented.

3.2 Description of the Experimental Setup

The specimens used by Kruger and Cvitkovich (1999) composed of a 203.2 mm x 25.4 mm skin and a 52 mm x 25.4 mm tapered flange, as shown in Figure 3-1. This tapered assembly was representative of a stringer (or flange) bonded to a composite skin. Secondary bonding was used to manufacture the specimens. Skin and flange components were cured separately, and then the cured components were post cured via an additional adhesive. The components were manufactured from IM6/3501-6 graphite/epoxy prepreg tape with an average ply thickness of 0.188 mm and bonded with Cyctec 1515 which had a cured thickness of 0.102 mm.

Both the skin and the flange laminates had a multi-directional lay-up. 0 axis in the lay-up was co-linear with the actuation direction. The skin was composed of 14 plies and the lay-up was $(0/45/90/-45/45/-45/0)_s$. On the other hand, the flange had 10 plies with a lay-up of $(45/90/-45/0/90)_s$. The mechanical properties of the composite and adhesive are presented in Table 3-1.

Test specimens were equipped with two strain gauges, one in the middle of the flange and the other on the skin close to the flange taper. The locations of the strain gauges could be seen on Figure 3-1.

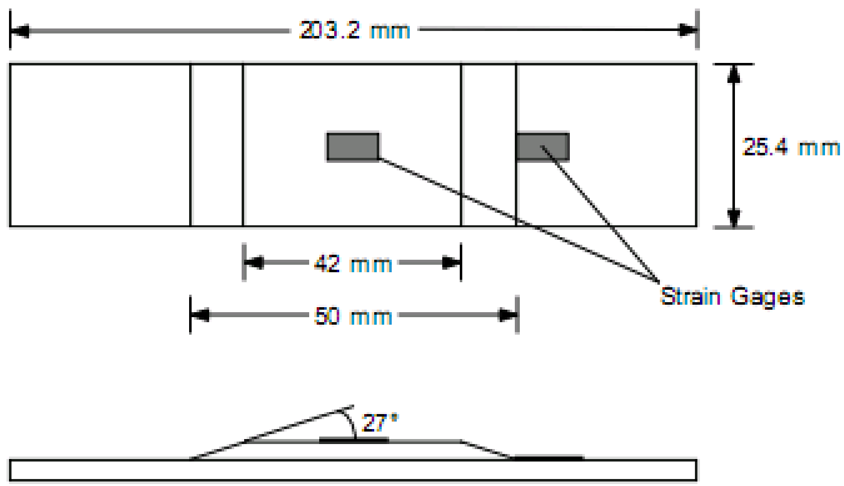

Figure 3-1: Schematic presentation of the specimens used by Krueger and Cvitkovich (1999)

Table 3-1: Material properties

Composite		Adhesive	
E_{11}, E_{22}, E_{33} (GPa)	144.70, 9.65, 9.65	E (GPa)	1.72
G_{12}, G_{13}, G_{23} (GPa)	5.20, 5.20, 3.40	ν	0.3
ν_{12}, ν_{13}, ν_{23}	0.30, 0.30, 0.45	t (mm, cured)	0.102
t (mm)	0.188		

Five displacement controlled quasi–static tension tests were performed using a servo-hydraulic load frame. The actuator displacement rate used in the experiments was 1.52 mm/min. The coupons were mounted in hydraulic grips of the test frame with a gage length of 127 mm. An extensometer was mounted on the specimen centering the flange taper. The schematic presentation of the experimental setup used by Kruger and Cvitkovich (1999) is shown in Figure 3-2.

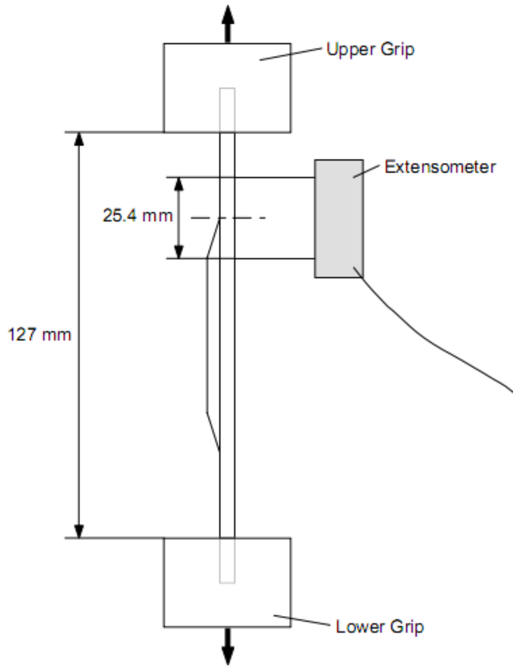

Figure 3-2: Schematic presentation of the experimental setup used by Krueger and Cvitkovich (1999)

3.3 Description of the Experimental Results

The force-deformation plots created using the actuator and extensometer displacements along with the observed force-surface strain plots are depicted in Figure 3-3 and Figure 3-4 respectively. The tests were terminated when a visual debond occurred between the skin and one of the flange tips.

As can be seen from the curves presented in Figure 3-3 and Figure 3-4, the initial response of the specimen is almost linear, that is, linear elastic. Formation of the first delamination is clearly marked in these figures. The observed response when delamination is initiated is a "snap through" response, which usually is observed when slender steel components undergo global (Euler) buckling. Nonetheless, after the formation of the (first) delamination, the component can take approximately 10% more axial load, and finally fails when debonding occurs. The observed response was similar for the five tested specimens (Krueger and Cvitkovich 1999). The average force and strain values observed during the five tests at the initiation of delamination and flange debond are tabulated in Table 3-2.

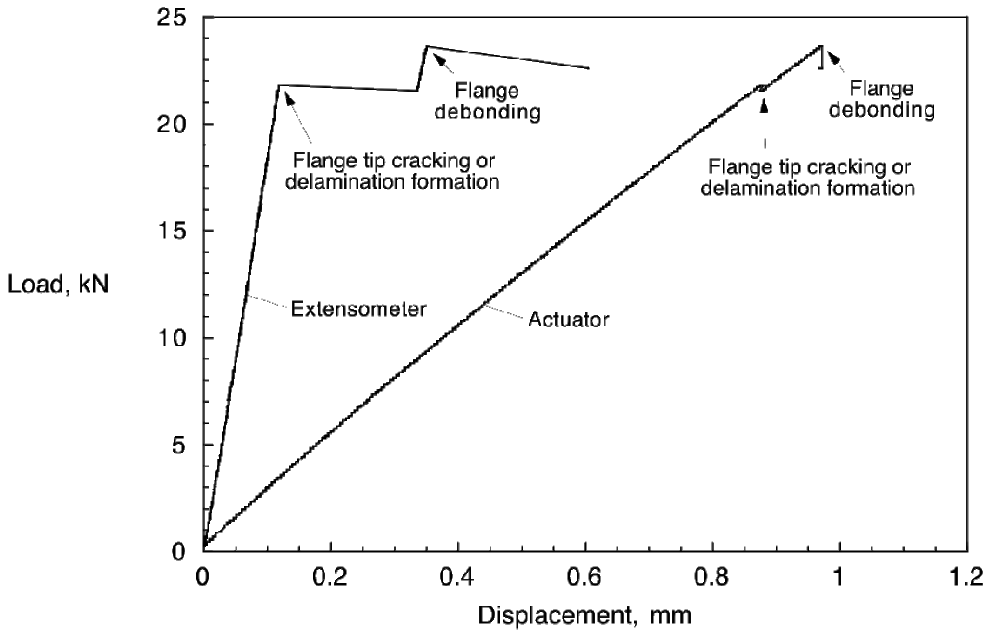

Figure 3-3: Force-deformation curves observed during the tension experiments (Krueger and Cvitkovich 1999)

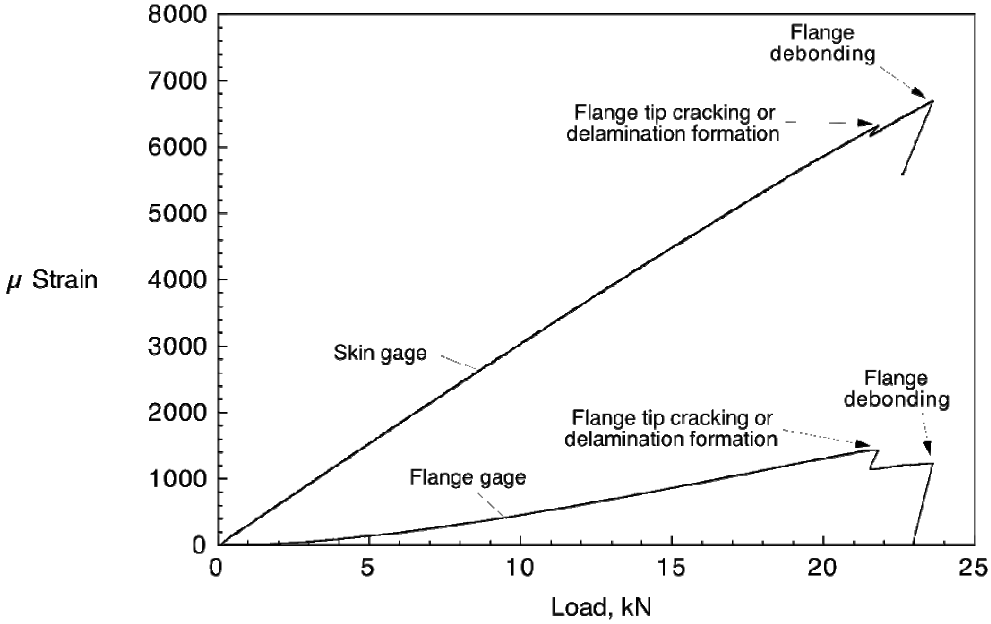

Figure 3-4: Force-strain curves observed during the tension experiments (Krueger and Cvitkovich 1999)

Table 3-2: Summary of the experimental results observed for the five tension specimens (Krueger and Cvitkovich 1999)

	Mean
Load at Damage initiation, kN	20.9
Flange strain at Damage initiation, με	1298
Skin strain at Damage initiation, με	5982
Load at flange debond, kN	22.7
Flange strain flange debond, με	1248
Skin strain flange debond, με	6385

Krueger and Cvitkovich (1999) observed that opposite corners of the flange debonded similarly. The nomenclature along with the schematic presentation of the damage observed during the experiments is shown in Figure 3-5, whereas the microscopic views of the debonding damage observed are depicted in Figure 3-6.

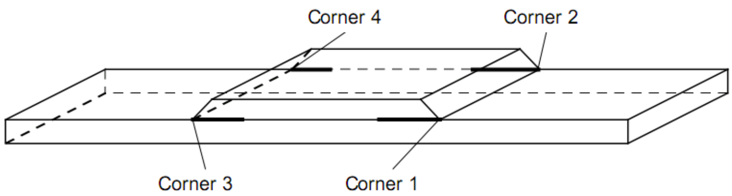

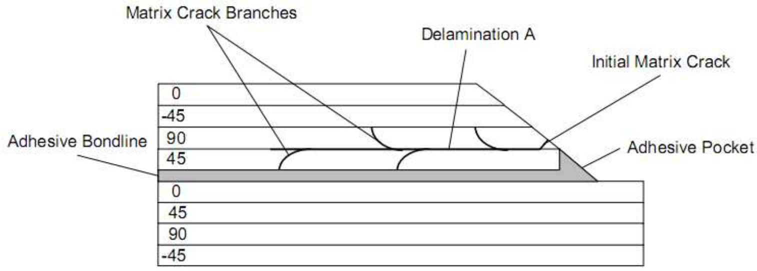

(a) Corners 1 and 4

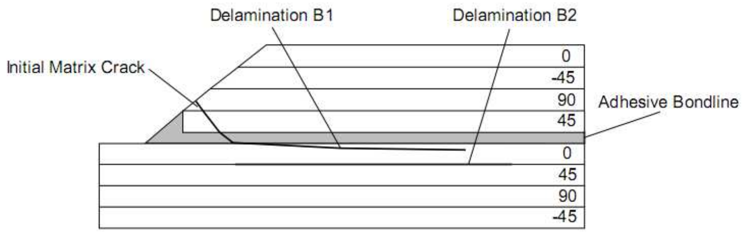

(b) Corners 2 and 3

Figure 3-5: Schematic presentation of the damage observed during the tension experiments (Krueger and Cvitkovich 1999)

(a) Delamination A in the 90°/45° Flange Ply Interface at Corner 4

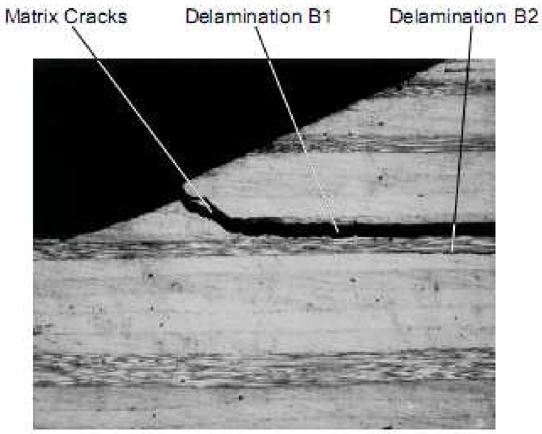

(b) Delamination B1 in the Top 0° Skin Ply and Beginning of Delamination B2 in The top 0°/45° Skin Ply Interface at Corner 2

Figure 3-6: Microscopic view of the debonding damage observed during the tension experiments (Krueger and Cvitkovich 1999)

3.4 Mixed-Mode Failure Criterion

The components tested by Krueger and Cvitkovich (1999) were manufactured from IM6/3506-1 graphite epoxy. A bilinear mixed mode failure criterion was proposed by Reeder (1993), O’Brien (1998) and Krueger and Cvitkovich (1999) for AS4/3501-6, which is a material similar to IM6/3506-1. The mixed mode failure criterion is shown in Figure 3-7. In Figure 3-7, the G_c value corresponding to G_{II}/G_T equal to zero represents the mode I fracture toughness value; while the G_c value corresponding to G_{II}/G_T equal to unity represents the mode II fracture toughness value. The values in between zero and unity for G_{II}/G_T represent different mixed-mode ratios.

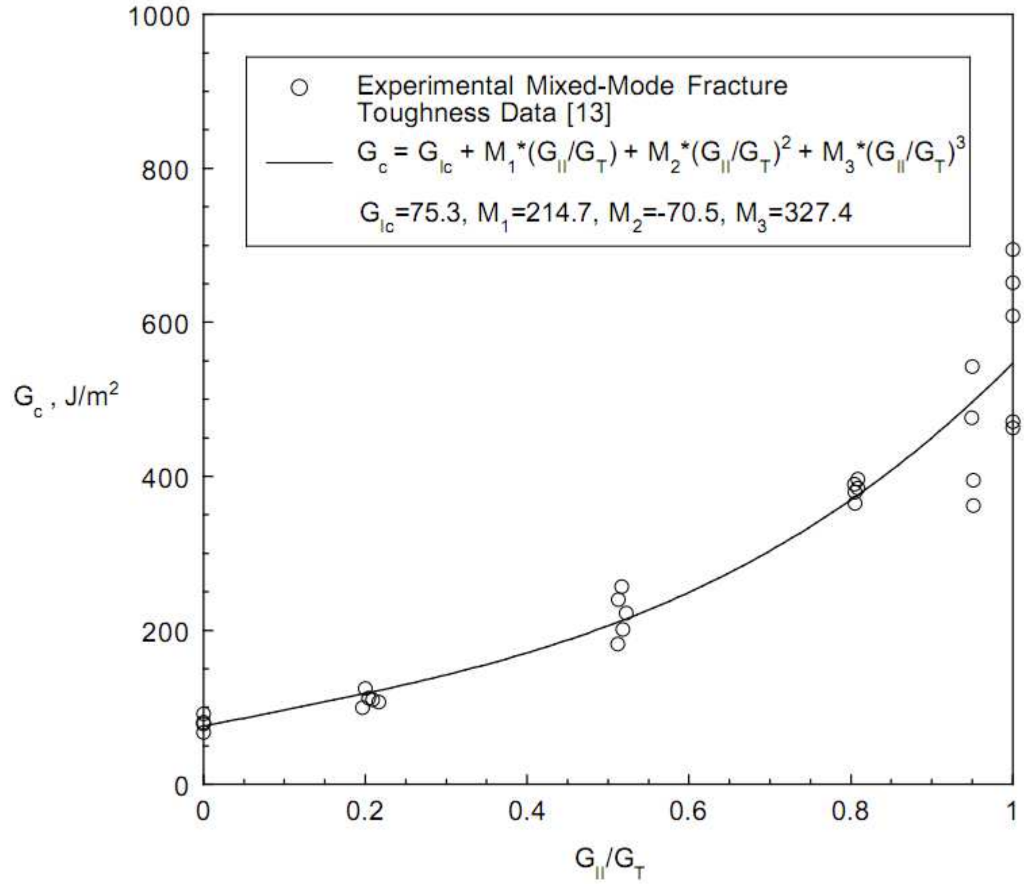

Figure 3-7: Mixed-mode delamination criterion for AS4/3501-6 (Krueger and Cvitkovich 1999)

A least square regression cubic curve fit to the mixed-mode failure criterion depicted in Figure 3-7 is as Krueger and Cvitkovich (1999):

$$G_c = 75.3 + 214.7\left(\frac{G_S}{G_T}\right) - 70.5\left(\frac{G_S}{G_T}\right)^2 + 327.4\left(\frac{G_S}{G_T}\right)^3 \qquad \text{3-1}$$

where G_c, G_s and G_t are the total fracture toughness, total shear energy release rate and total energy release rate values respectively. For 2D models the total shear energy release rate, G_s is equal to mode II energy release rate due to the fact that mode III energy release rate equals to zero. For 3D models the total shear energy release rate, G_s is equal to the sum of mode II and mode III energy release rates.

CHAPTER 4

FINITE ELEMENT RESULTS

In this chapter, details of the finite element models (FEM) used in this study are described and the results of the study are presented. During the course of work, Abaqus/CAE 6.10 is used as pre & post-processor and solver. Phyton scripts are generated to extract the results, and the extracted data is post-processed using Microsoft Excel.

At first the global response of the undamaged specimen is investigated. This was done to compare the results of different FE modeling techniques with the experimental results. The specimens tested by Kruger and Cvitkovich (1999) are chosen as benchmark examples, which were explained in detail in Chapter 3. In the undamaged specimen no delaminations or debondings are embedded into the FEM. The nodes, where the delamination was observed in the experiments are connected with rigid multi-body constraints (MPC). This technique is preferred for the subsequent delamination analysis in order to ease the analysis of delamination onset. Separate finite element models consisting of 2D plane stress solid elements, 2D plane strain solid elements and 3D solid elements are used. The results obtained from each model are compared with the experimental ones. For 2D analyses the effect of element order is investigated by analyzing the same specimen with first order (linear) and higher order (quadratic) elements. For 3D analyses the effect of mesh density is investigated by analyzing the specimen with fine and coarse meshed models. Both linear and geometric nonlinear analyses are conducted to compare the effect of geometric nonlinearity. Material nonlinearities are beyond the scope of this study.

After the specimen global response is validated, virtual crack closure analyses is conducted. Again, separate finite element models consisting of 2D plane stress solid elements, 2D plane strain solid elements, and 3D solid elements are considered to investigate the effect of modeling technique. Similar to the global response study, for 2D elements the effect of element order and for 3D analyses effect of mesh density is investigated. Based on the results obtained from global response study, only geometrical non-linearity is considered for virtual crack closure analyses.

Finally, the effect of (initial) defect or flaw location on the delimination growth potential is investigated using 3D finite element models. Particularly, two cases are studied; the effect of a (initial) defect or flaw that might have occurred at the free edge, and the one that might have occurred at the center of the assembly. This is done by embedding some initial defects into the 3D finite element model and comparing the delamination growth potentials. Models with different mesh densities are considered to study the effect of different modeling techniques.

4.1 General Description of the 2D Finite Element Models

For the 2D plane stress and 2D plane strain finite element models the same mesh, boundary conditions and material properties are used, while the element types and formulations (orders) are changed accordingly. The total length of the specimen modeled was 127 mm, which corresponds to the specimen between the hydraulic grips of the servo-hydraulic load frame.

For the 2D models (plane stress and plane strain) the cross-section of the specimen used is shown in Figure 4-1. The primary fiber direction (0 degree) is co-linear with the x-axes of the global coordinate system and the cross-section of the specimen is in the x-y plane of the global coordinate system as depicted in Figure 4-1.

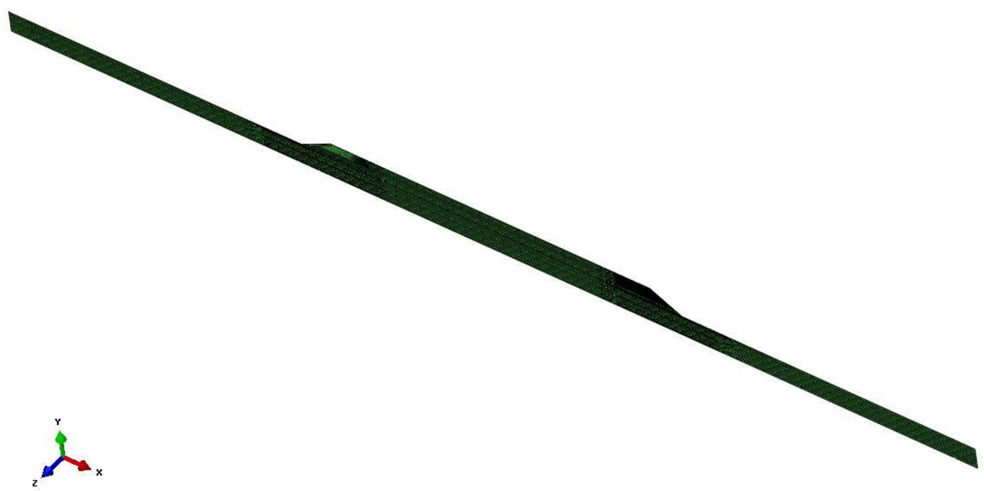

Figure 4-1: 2D FE models of the test specimen

In the region of interest, where the delamination occurs, the first two plies closer to the adhesive and the adhesive region are modeled with four elements through thickness. In the far field, the plies are modeled with one element. This refinement and transition is done, to obtain a feasible solution without sacrificing the accuracy of the model. The global mesh and the mesh in the region of interest are given in Figure 4-1 and Figure 4-2 respectively.

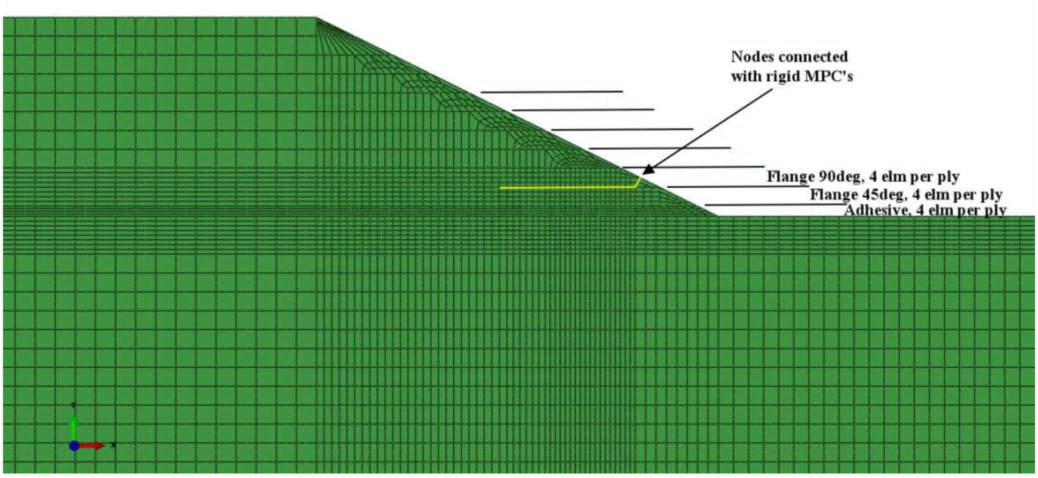

Figure 4-2: Details of the mesh in the region of interest

The 2D models are composed of 8022 elements, where 7975 of them are quadrilateral, and the rest are triangular. The triangular elements are located far from the region of interest in order to have a better accuracy. The 2D models with quadratic elements consisted of 24583 nodes, while the models with linear elements are composed of 8260 nodes.

4.1.1 2D Plane Stress FE Analyses

Plane stress elements are preferred when the thickness of the body is small relative to the in-plane dimensions. The stresses are functions of planar coordinates alone and out-of-plane normal stress ($\sigma_{33}=0$), and shear stresses ($\tau_{13}=\tau_{23}=0$) directed perpendicular to the x-y plane are zero.

Two sets of analyses, with two different types of elements are conducted, to investigate the effect of element order (linear versus quadratic). The difference between first order (linear) and higher order (quadratic) elements is depicted in Figure 4-3. In the first set, the specimen is modeled with eight-node bi-quadratic reduced integration plane stress quadrilateral (CPS8R) and six-node modified with hourglass control plane stress triangle (CPS6M) elements. In the second set, the specimen is modeled with four-node bilinear plane stress quadrilateral (CPS4), and three-node bilinear plane stress triangle (CPS3) elements.

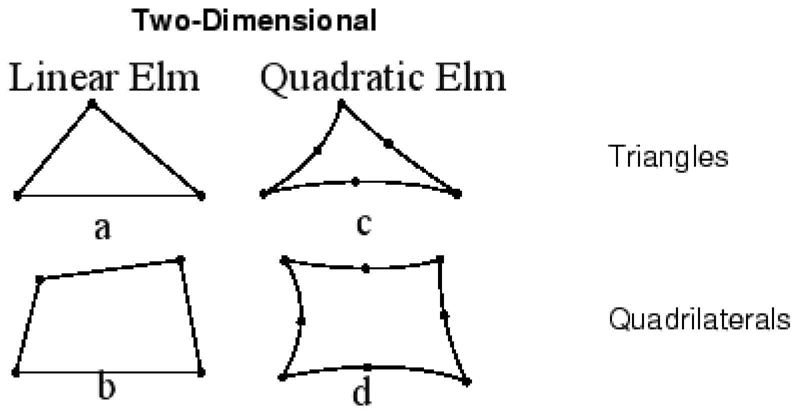

Figure 4-3: 2D element types (Abaqus 2010)

In the model the thickness of the section is assumed to be 0.1 mm. The results obtained from the FE analyses are multiplied by 254 (*=25.4/0.1*), to calculate the total load.

4.1.2 2D Plane Strain FE Analyses

Plane strain elements are preferred when the strains in a loaded body are functions of planar coordinates alone and the out-of-plane normal (ε_{33}) and shear strains (γ_{13} and γ_{23}) are equal to zero. In plane strain elements all loading and deformations are restricted to the x-y plane.

Again, two sets of analyses with two different types of elements are conducted, to investigate the effect of element order (see Figure 4-3). In the first set, eight-node bi-quadratic reduced integration plane strain quadrilateral (CPE8R), and six-node modified with hourglass control plane strain triangle (CPE6M) elements are used. In the second set, four-node bilinear plane strain quadrilateral (CPE4), and three-node bilinear plane strain triangle (CPE3) elements are used.

Both 0.1 mm and 25.4 mm section thickness values are analyzed in order to investigate the effect of assumed thickness. In the model with 0.1 mm section thickness, the results obtained from the FE analyses are multiplied by 254 (*=25.4/0.1*), to calculate the total load.

4.1.3 Material Properties and Boundary Conditions used in the Finite Element Analyses

The adhesive is assumed to be isotropic and the composite laminate is assumed to be orthotropic. Since the x-axis of the global coordinate system is co-linear with 0 degree of the lay-up, orthotropic material properties of IM6/3501-6 unidirectional (UD) graphite/epoxy tape are directly used for the 0 degree lamina. For 45 and 90 degrees a coordinate transformation has done.

2D plane stress and 2D plane strain elements should be defined in x-y plane, hence the coordinate transformation for 45 and 90 degrees are done around the y axis. The direction-cosine matrix for a rotation in y direction of a Cartesian coordinate system, first proposed by Descartes (1637), is as:

$$a = \begin{bmatrix} \cos\theta & 0 & \sin\theta \\ 0 & 1 & 0 \\ -\sin\theta & 0 & \cos\theta \end{bmatrix} \qquad 4\text{-}1$$

In Equation (4-1) a represents direction-cosine matrix, and θ is the angle of rotation. The transformation of the stiffness matrix (C) is as:

$$C' = MCM^T \qquad 4\text{-}2$$

where C' is the stiffness matrix in the transformed coordinate system; T denotes transformation of the matrix; and M is a (6,6) matrix whose details are described below:

$$M = \begin{bmatrix} M_{11} & M_{12} \\ M_{21} & M_{22} \end{bmatrix} \qquad 4\text{-}3$$

where:

M_{11}: The *(i,j)* component is equal to the square of the *(i,j)* component of a^T. (ie: $M_{11}(1,1)= a_{11}^2$);

M_{12}: The *(i,j)* component is equal to twice the product of the other terms of the row i of a^T. (ie: $M_{12}(1,1)=2*a_{21}*a_{31}$);

M_{21}: The *(i,j)* component is equal to the product of the two other terms of the column j of a^T. (ie: $M_{21}(1,1)=a_{12}*a_{13}$);

M_{22}: The *(i,j)* component is equal to the sum of the cross products of the terms of the matrix obtained by removing row i and column j of a^T. (ie: $M_{22}(1,1)= a_{22}*a_{33}+a_{32}*a_{23}$).

One side of the specimen is fixed in translation and rotation directions and on the other side 22.7 kN of load is applied in the positive x axis of the global coordinate system in order to simulate the actuation of the hydraulic grips. The transverse displacements and rotations are also fixed; since during the test, the load frame preserves transverse motion of the grips. The rotation in the edges is also fixed due to the fact that a comparatively long piece of specimen (specimen tab) is clamped in the hydraulic grip. The applied boundary conditions could be seen in Figure 4-4.

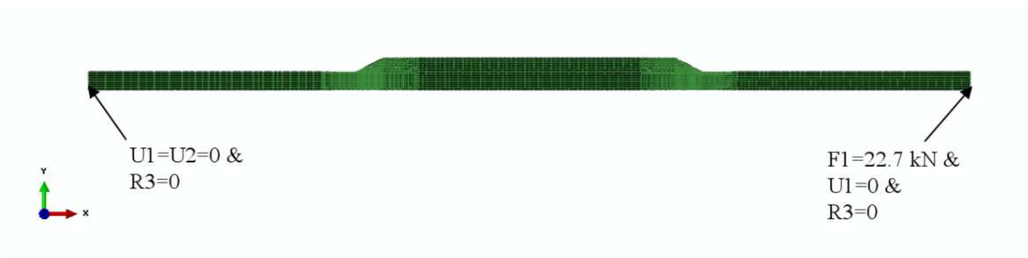

Figure 4-4: Boundary conditions of 2D models

In the global response analysis, it is assumed that no failure (as delamination or debonding) occurred during the loading and the maximum applied load is incremented into 10 equal segments.

As described in the beginning of this chapter, the delamination region observed in the test specimen is modeled via duplicated nodes connected by multi-point constraints (MPC). During the delamination onset analysis, each multi-point constraint is individually released, illustrating the onset of the current delamination to the succeeding MPC. After the release of each MPC, separate geometrically non-linear analyses are conducted to calculate the strain energy release rates at that specific delamination length.

4.2 General Description of the 3D Finite Element Models

The 3D finite element model is generated by the extrusion of the 2D models by 25.4 mm specimen thickness. Two 3D models are constructed in order to benchmark the effect of mesh size on the result:

- The first 3D model consisted of 10 rows of equally spaced elements through thickness of the specimen The isometric and through depth views of the coarse 3D model are depicted in Figure 4-5 and Figure 4-6 respectively,

- On the other hand the second model had a fine mesh in the free edge zones with sixteen rows of elements through depth. The 1 mm near edge field of the specimen is modeled with four elements through thickness and the remaining middle side is modeled with eight elements giving sixteen element rows through depth. It is aimed to capture the gradient in the free edges with the fine mesh model. The isometric and through depth views of the coarse 3D model are depicted in Figure 4-7 and Figure 4-8 respectively.

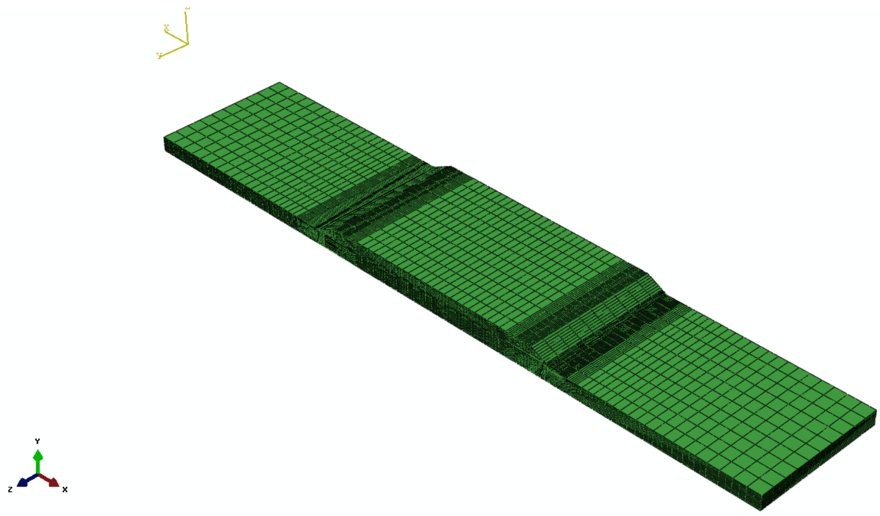

Figure 4-5: Isometric view of the coarse 3D FE model of the specimen

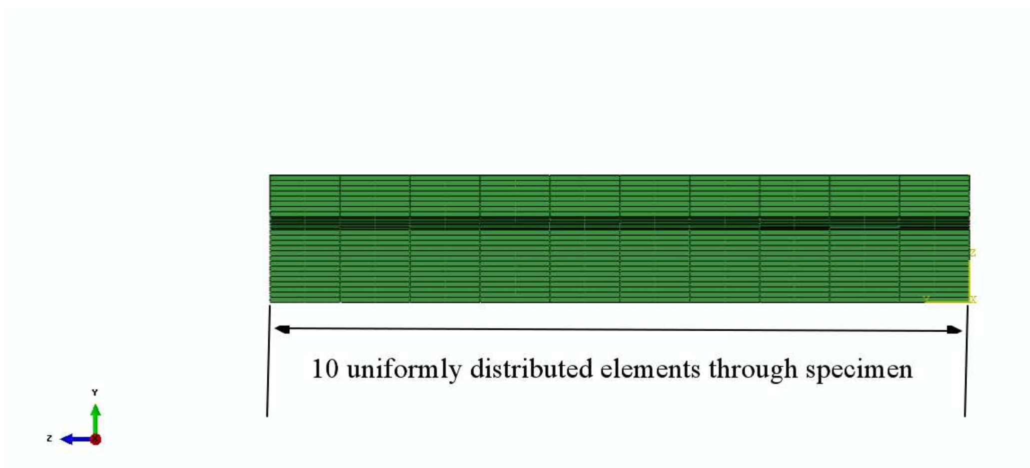

Figure 4-6: Through depth view of the coarse 3D FE model of the specimen

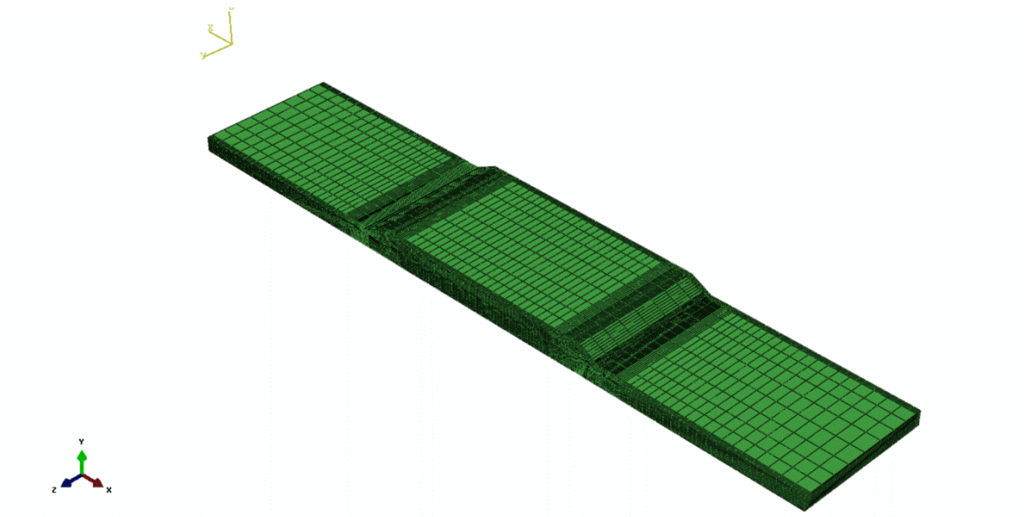

Figure 4-7: Isometric view of the fine 3D FE model of the specimen

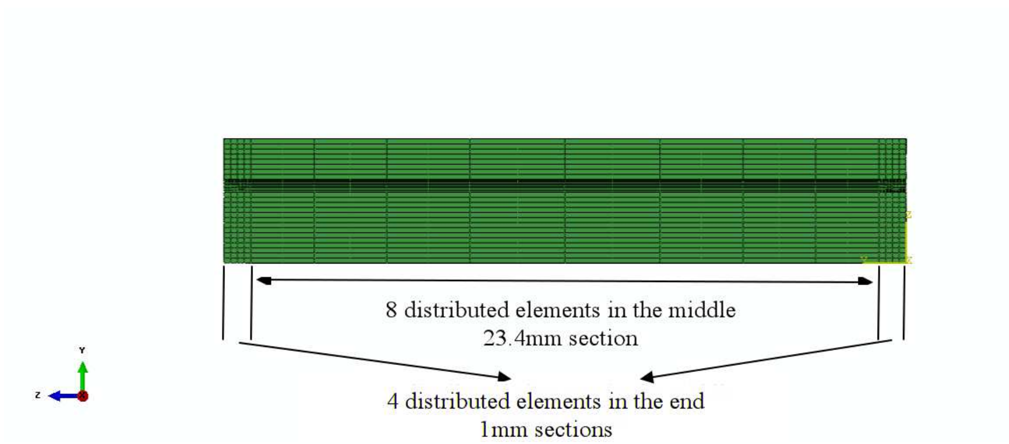

Figure 4-8: Through depth view of the fine 3D FE model of the specimen

In both 3D models the 0 degree lamina is co-linear with the x-axis of the global coordinate system of the finite element models shown in Figure 4-5.

Based on the results obtained from 2D analyses, only 3D models consisting of higher order (quadratic) elements are considered. However, two sets of analyses are conducted to investigate the effect of mesh density. Both models consisted of twenty-node quadratic brick (C3D20), and fifteen node quadratic triangular prism (C3D15) elements. C3D20 and C3D15 elements are depicted in Figure 4-9(f) and Figure 4-9(e) respectively. The coarse 3D model is composed of 352496 nodes and 80170 elements, of which 79700 are hexahedral. The fine 3D model is composed of 549272 nodes and 28272 elements, where 127520 of them are hexahedral elements. In both 3D models the wedge elements are located far from the region of interest in order not to reduce the accuracy of the results.

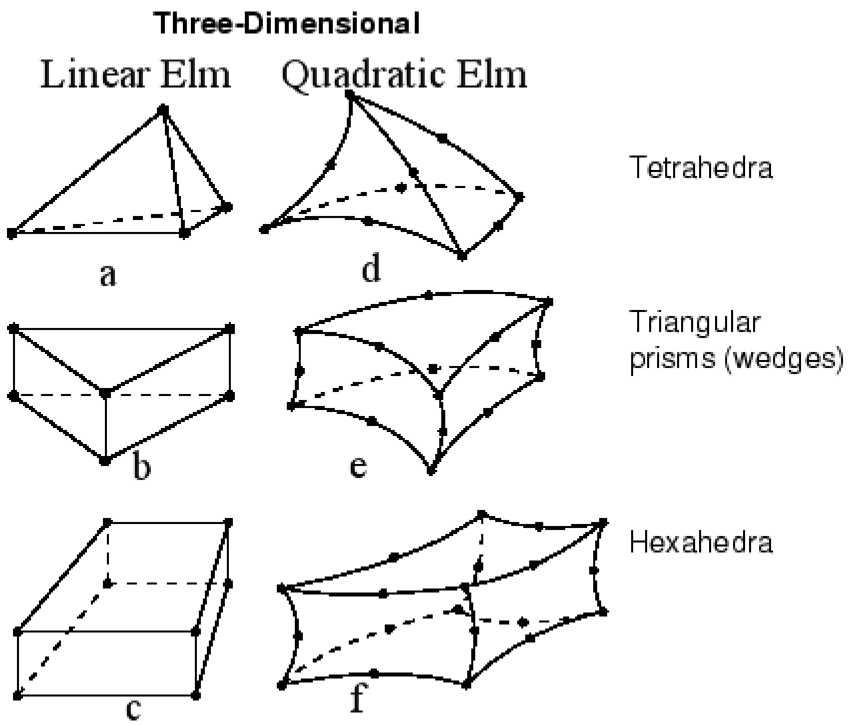

Figure 4-9: 3D element types (Abaqus 2010)

4.2.1 Material Properties and Boundary Conditions used in the 3D Finite Element Analyses

The adhesive is assumed to be isotropic, and the composite laminate is assumed to be orthotropic as in the 2D model. A coordinate system is defined for material assignment as shown in Figure 4-10. A transformation is done with respect to the z axis of the material transformation coordinate for 45 and 90 degree lamina.

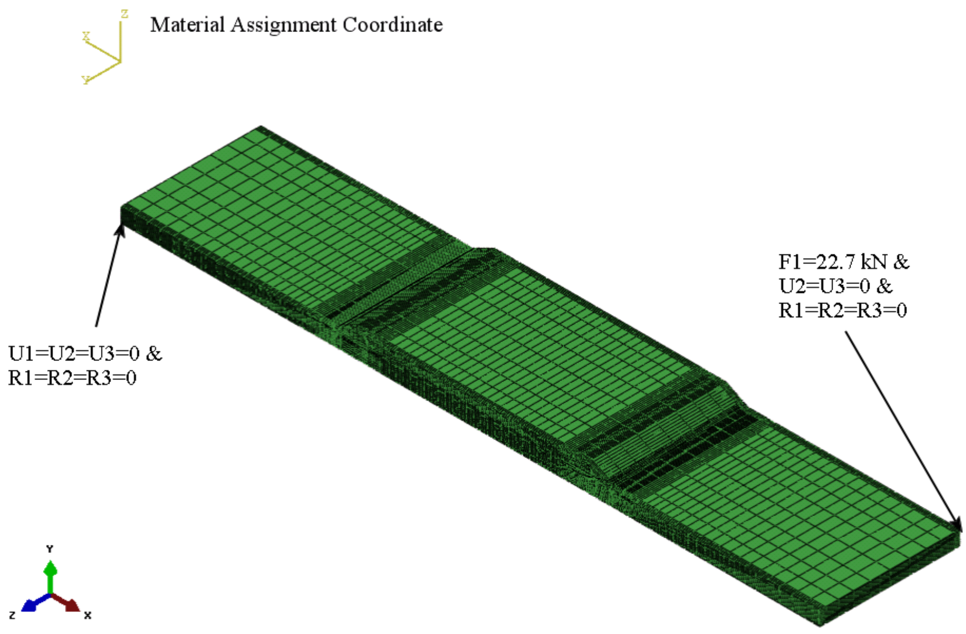

Figure 4-10: Material assignment coordinate and boundary conditions of 3D model

Boundary conditions used for the 3D models are similar to the ones used for the 2D models. In addition to the constraints applied in the 2D model, z translation, y and z rotations are also fixed in the 3D models. The boundary conditions are applied to all nodes through the thickness of the 3D models. The applied boundary conditions of the 3D model could be seen in Figure 4-10.

4.3. Results

In this subsection the results of the global response analysis are presented for the 2D and 3D models. After the global response analysis results the VCCT results are presented.

4.3.1 Global Response Results

During the global response analysis, the calculated results are compared with the ones reported by Kruger and Cvitkovich (1999) (see also Chapter 3). Several parameters are investigated during the scope of the work:

1) effect of different modeling techniques; such as 2D plane strain, 2D plane stress and 3D models;
2) effect of geometric non-linearity;
3) effect of element order, i.e.: linear elements and quadratic elements;
4) effect of mesh density.

4.3.1.1 Effect of Modeling Techniques

The comparison of the predicted force displacement response obtained from the 2D plane strain, 2D plane stress and 3D analyses, with the experimental one is presented in Figure 4-11. The displacement extracted from the finite element models is, in the vicinity where the extensometer is attached to the test specimen. The results presented in Figure 4-11 are obtained with geometrically non-linear analyses, and using higher order (quadratic) elements. As can be seen from Figure 4-11, the non-linear 3D models are very close to the test results. A slight difference in the force-deformation response is observed for the fine and coarse FE models. The non-linear 2D plane strain model yields a little stiffer specimen, and the 2D plane stress model yields a little softer specimen. It must also be noted that the same global response is observed for the 2D plane strain analyses, where the specimen is modeled as 0.1 mm and 25.4 mm thick. Figure 4-11 also indicates that plane strain and plane stress models form the upper and lower bounds of the analyses respectively from force displacement point of view.

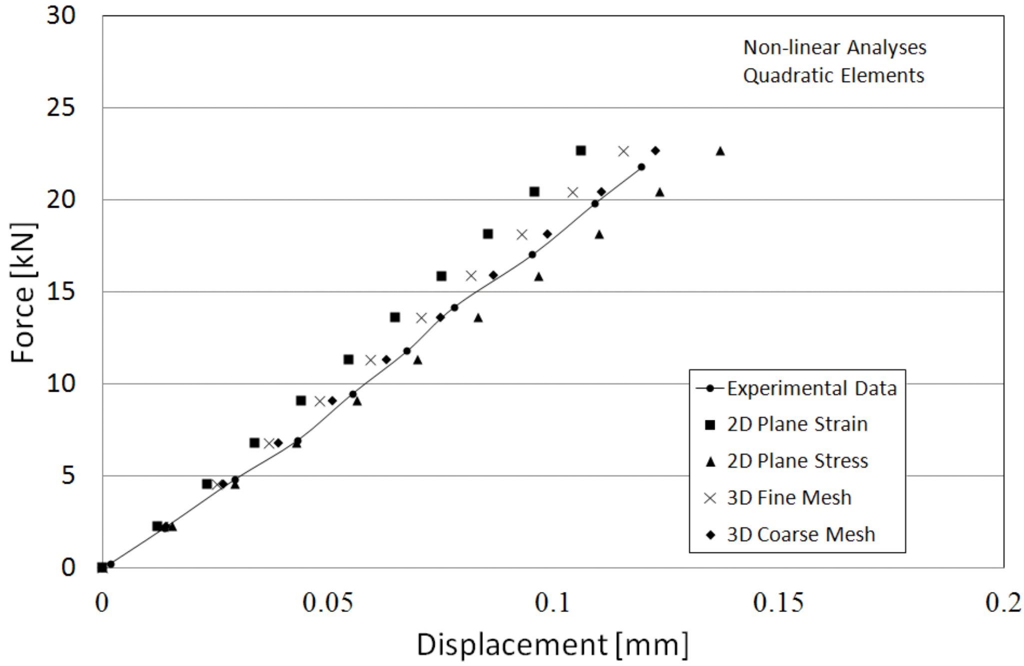

Figure 4-11: Force-displacement relation of non-linear analysis

The flange strain gauge data comparison is depicted in Figure 4-12. The 2D plane stress model deforms more, compared to the 2D plane strain model. While the results obtained from the plane strain analyses seem to be more realistic, the plane strain and plane stress models seem to form an upper and lower bounds. This behavior in the strain data is concurring to the behavior in the force-displacement data.

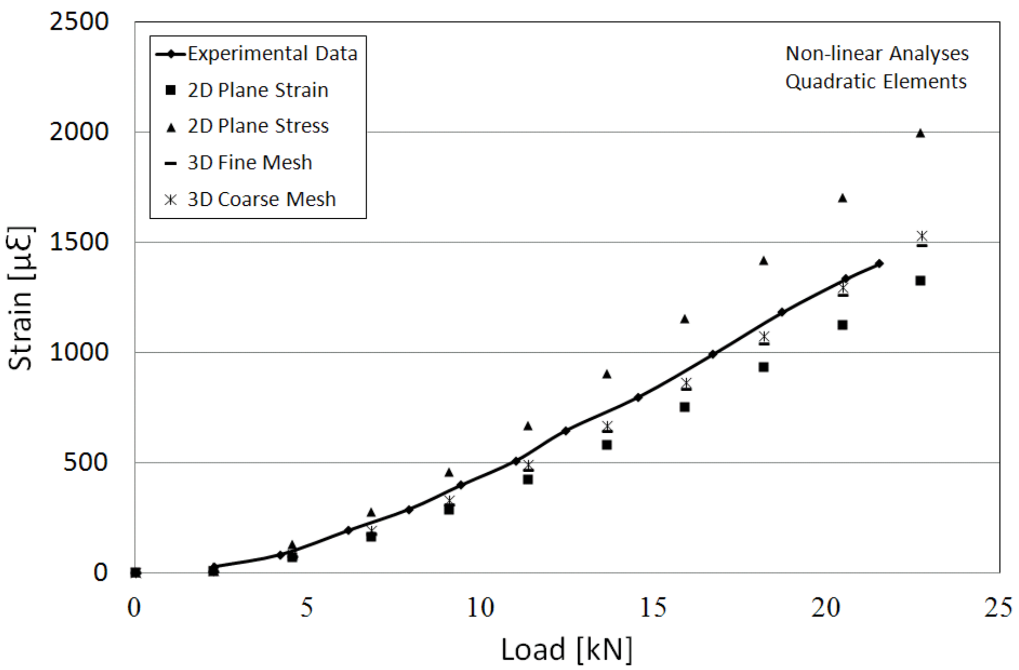

Figure 4-12: Force – strain relation at flange

4.3.1.2 Effect of Geometric Non-linearity

The deformation contour of geometric non-linear and linear plane strain model is depicted in Figure 4-13 and Figure 4-14 respectively. In Figure 4-13 and Figure 4-14 the upper deformed shape is the real deformation and the lower deformed shape is the deformation scaled by a factor of 5. As could be seen from the figures the models bend due to a shift in the neutral axis of the component at the flange skin connection.

Figure 4-13: Deformation contour of geometric nonlinear plane strain model

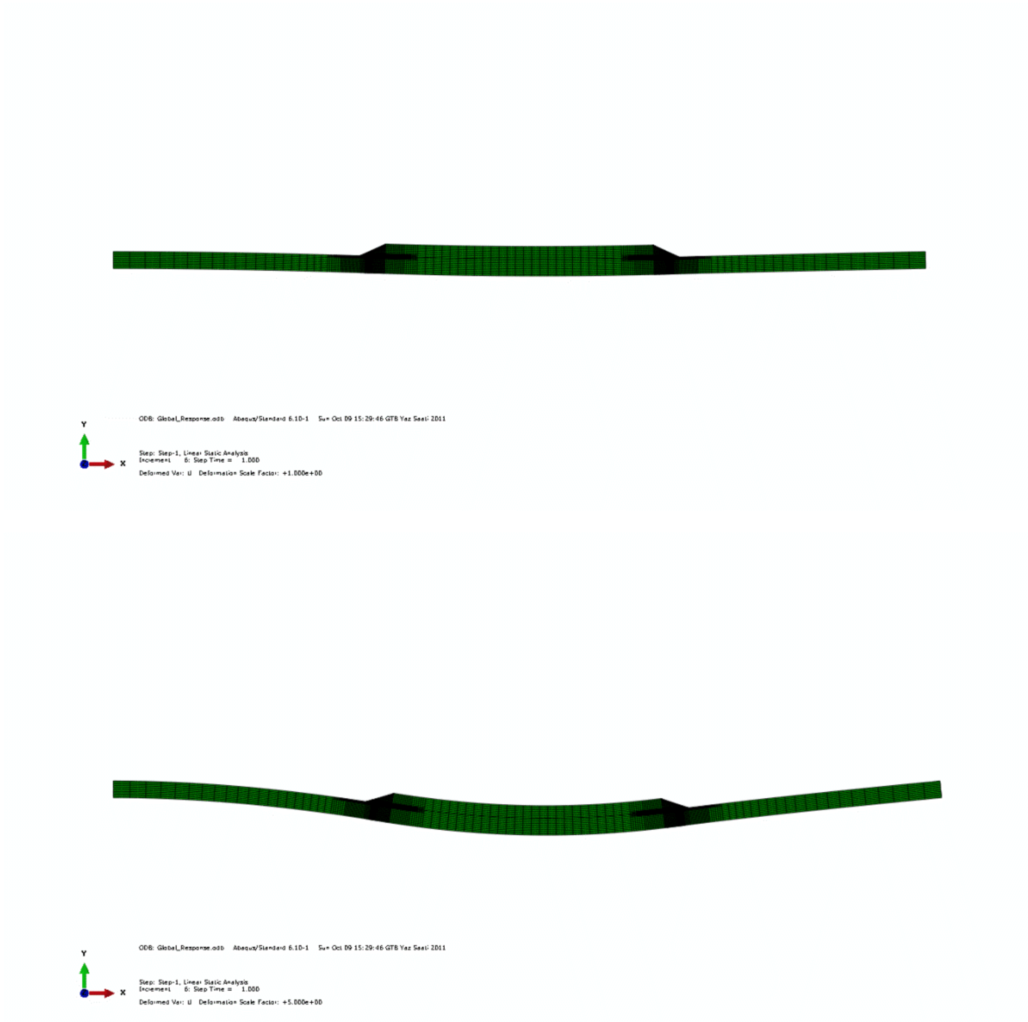

Figure 4-14: Deformation contour of geometric linear plane strain model

A comparison of the force-deformation, and strain-force curves obtained using geometric non-linear and linear analyses are depicted in Figure 4-15, Figure 4-16, Figure 4-17 and Figure 4-18. Organization of these figures are as follows: Figure 4-15, Figure 4-16 and Figure 4-17 present the comparison of the force-deformation relationships for 2D plane strain, 2D plane stress and 3D models respectively; and Figure 4-18 presents the flange strain gauge data comparison.

As can be seen from the force-displacement relationships (Figure 4-15, Figure 4-16 and Figure 4-17), while the difference between the linear and non-linear analyses is small, the linear analyses results in a softer specimen response. On the other hand, the importance of conducting a geometrically non-linear analysis is obvious from Figure 4-18. The comparison conducted at the flange of the specimens show that if a linear analyses is conducted the strain values obtained are unrealistic. This can be attributed to the fact that an excessive and unrealistic bending is observed in linear analysis, such that the normal strain caused by axial loading are eliminated by the normal strains caused by the excessive bending of the specimen. Hence a geometrically linear analysis is not recommended for these types of analyses with high deformations. For this reason the study is continued with geometrically non-linear analyses only.

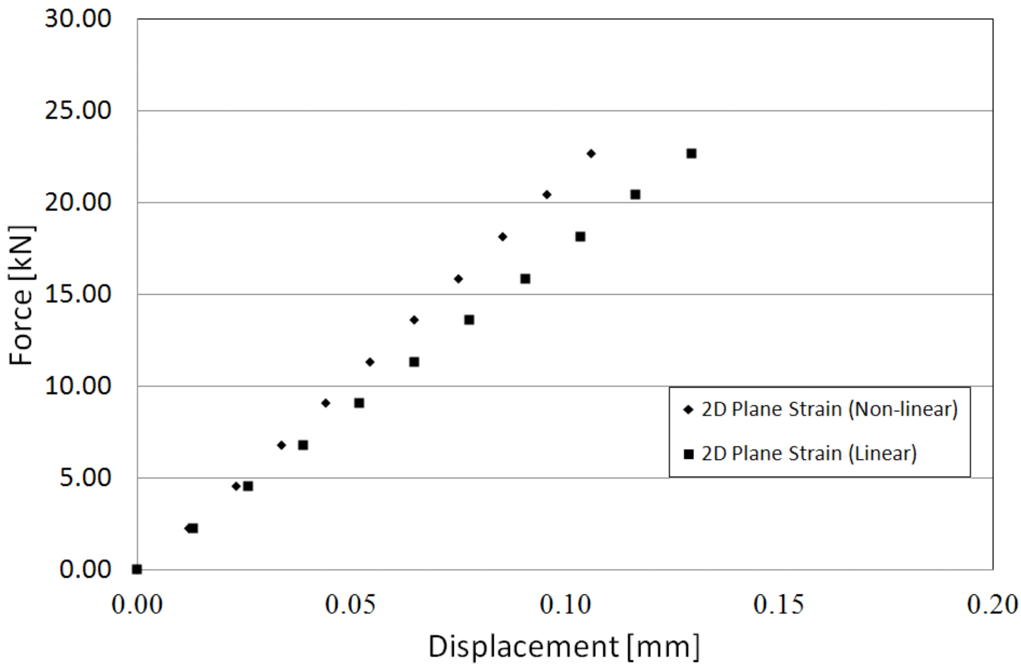

Figure 4-15: Linear vs. Nonlinear for 2D plane strain

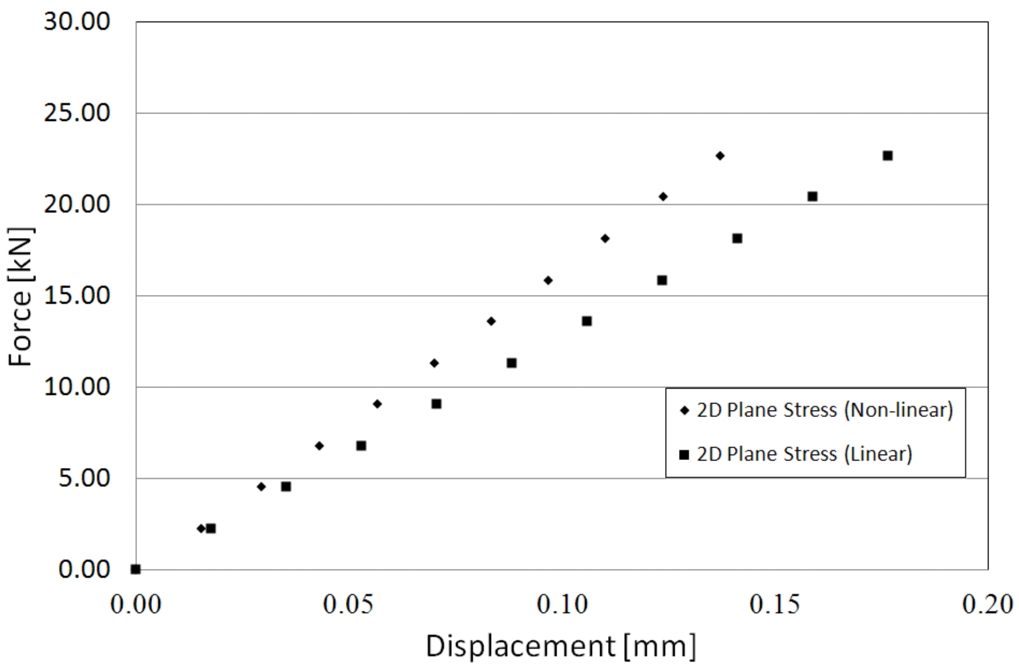

Figure 4-16: Linear vs. Nonlinear for 2D plane stress

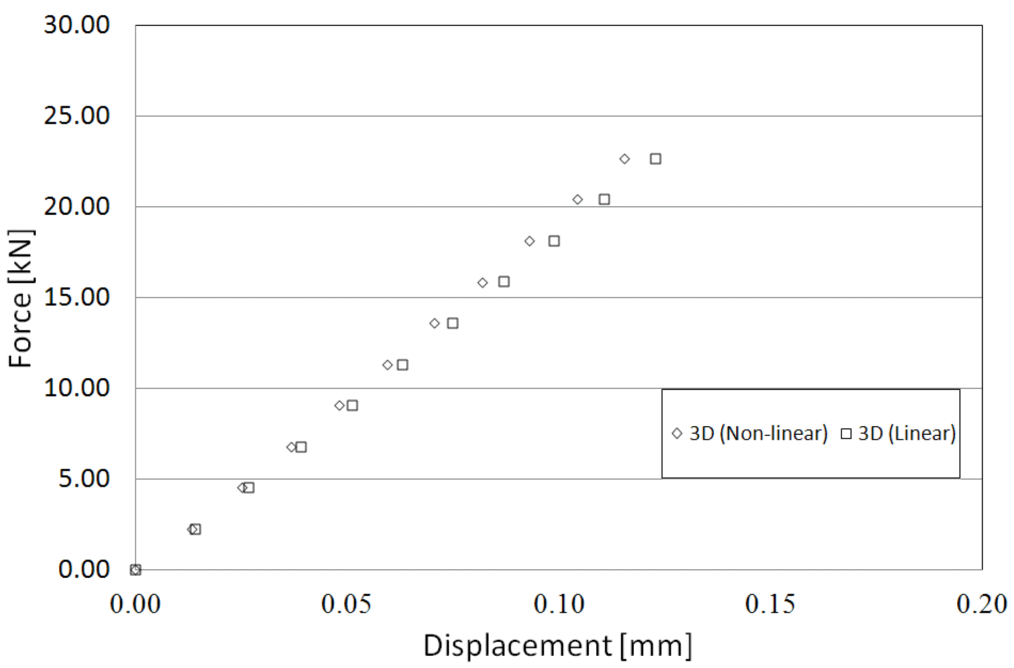

Figure 4-17: Linear vs. Nonlinear for 3D fine model

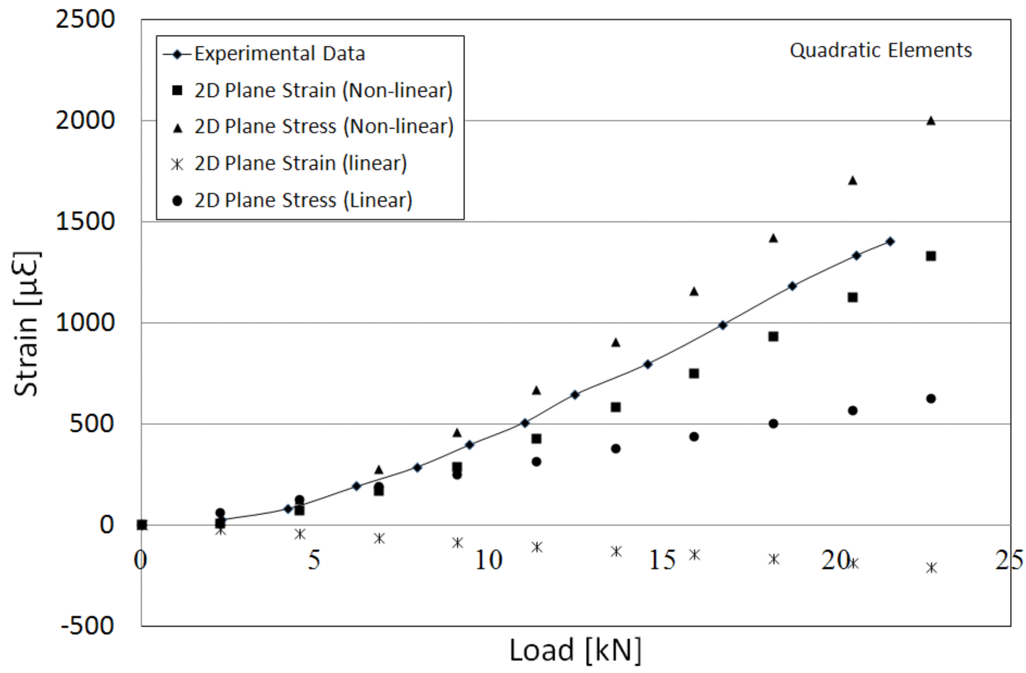

Figure 4-18: Force – strain relation at flange

4.3.1.3 Effect of Element Order for 2D Analyses

Both 2D models are analyzed with linear and quadratic elements in order to understand the effect of element order on the global response. The results are summarized in Figure 4-19 and Figure 4-20. An inspection of Figure 4-19 shows that the element order does not have a significant effect on the force-displacement relationship for both 2D plane strain and plane stress models. On the other hand, the strain data given in Figure 4-20 indicates that the effect of element order is not the same for 2D plane stress and plane strain analyses. For plane stress analyses strain time history predicted by linear and quadratic elements are the same, indicating no significant effect of element order. For plane strain analyses the model with linear elements tends to deform more than the one with quadratic elements. It should be noted that generally an analyses with quadratic elements will give more accurate results compared to the one with linear elements due to the node configuration (Abaqus 2010).

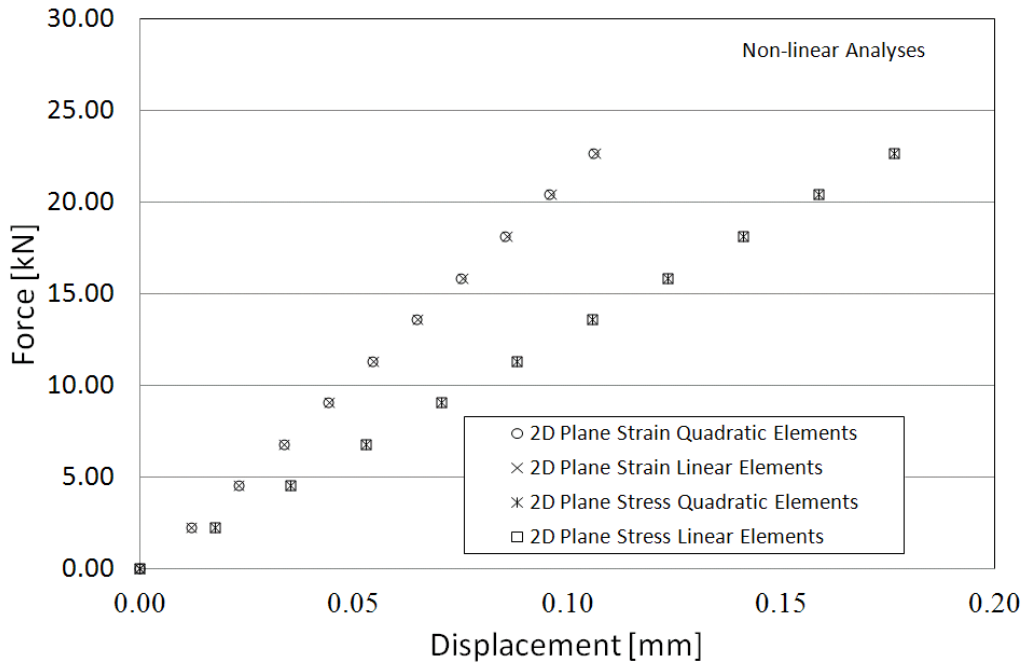

Figure 4-19: Force – Displacement relation comparison for element order

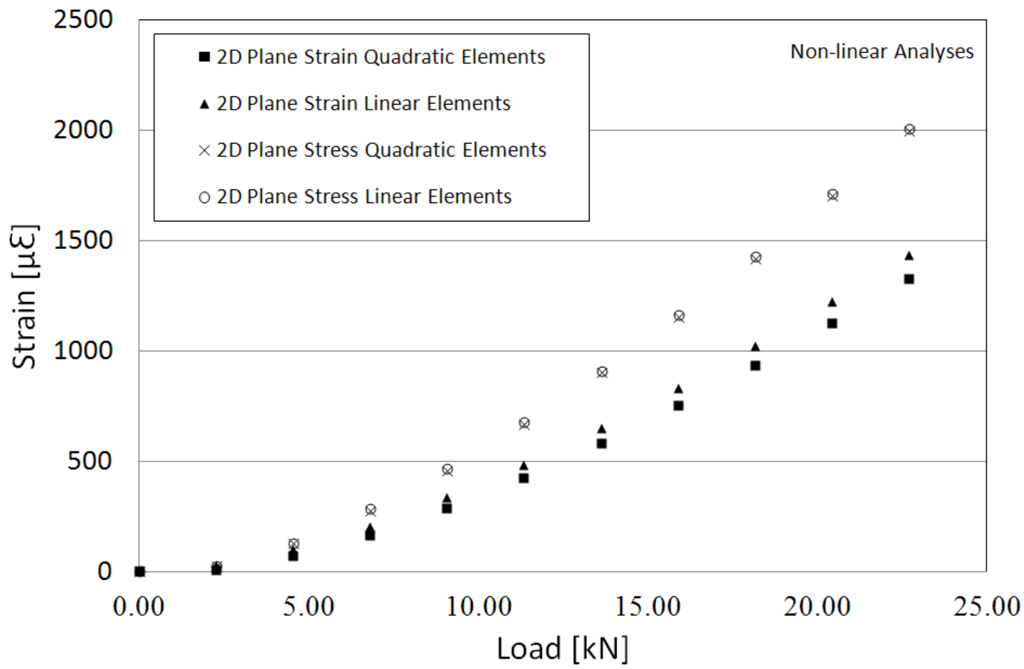

Figure 4-20: Flange strain variation due to element order

4.3.2 Strain Energy Results of VCCT

For the delamination formation and onset analysis several parameters are studied. The studied parameters are;

1) effect of different modeling techniques, such as 2D plane strain, 2D plane stress and 3D models;
2) effect of element order, that is, linear elements and quadratic elements;
3) effect of different multi-point constraints (MPC), such as all degrees of freedoms (DOF) are constraint at crack tip and just translational ones are constraint at crack tip;
4) effect of geometric non-linearity;

5) effect of mesh density on the free edges for the 3D models.

It must be noted that based on the results presented in Figure 4-18, it is concluded that geometrically linear analyses might result in un-realistic strain and deformation results. Therefore, only geometrically non-linear analyses are considered for the VCCT analyses.

4.3.2.1 Effect of Modeling Techniques

Comparison of calculated mode I, mode II and the total strain energy release rates for 2D plane stress, 2D plane strain and 3D analyses are presented in Figure 4-22, Figure 4-23 and Figure 4-24 respectively. The models are geometrically non-linear and the elements are quadratic elements. For the 3D model the strain values are extracted in the middle of the test specimen, which is depicted in Figure 4-21. It should be noted that for the 3D model, at the middle of the test specimen mode III energy (G_{III}) approaches to zero.

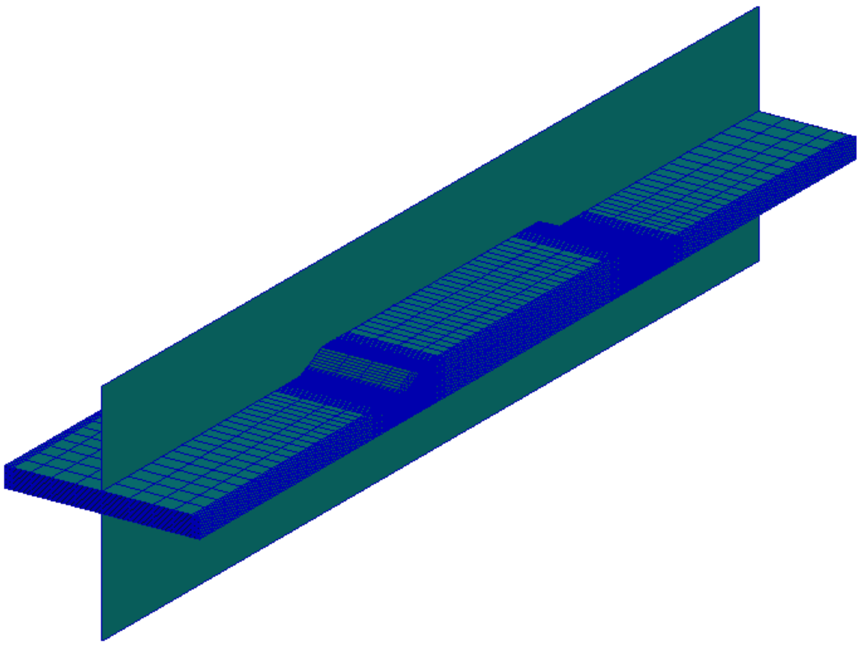

Figure 4-21: The 3D section used for comparison with 2D models

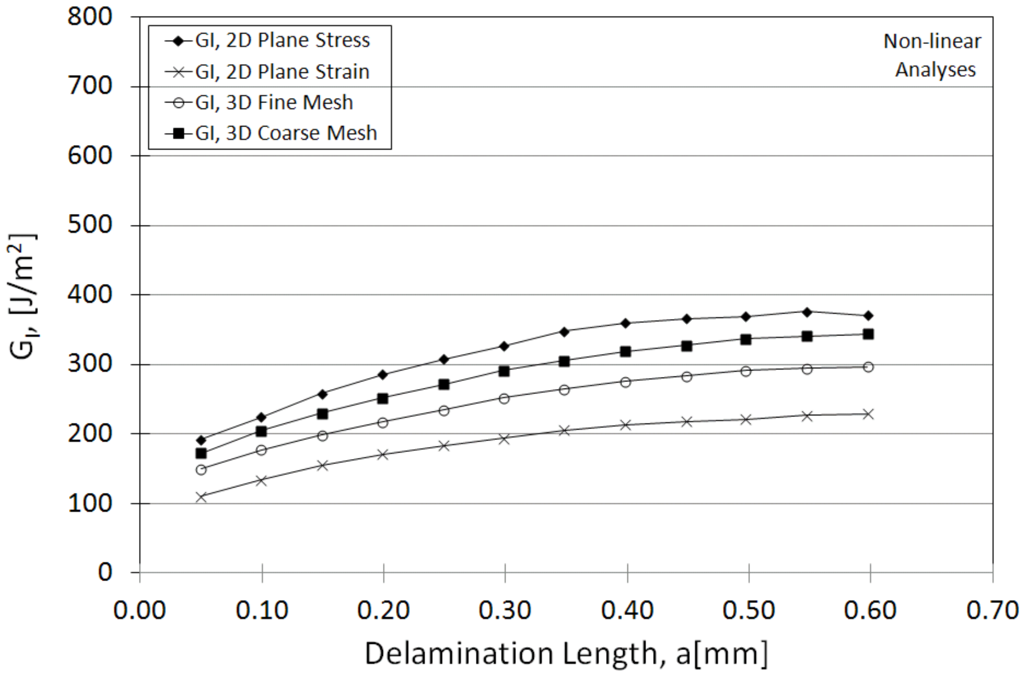

Figure 4-22: Comparison of G_I of 2D models and middle section of 3D models

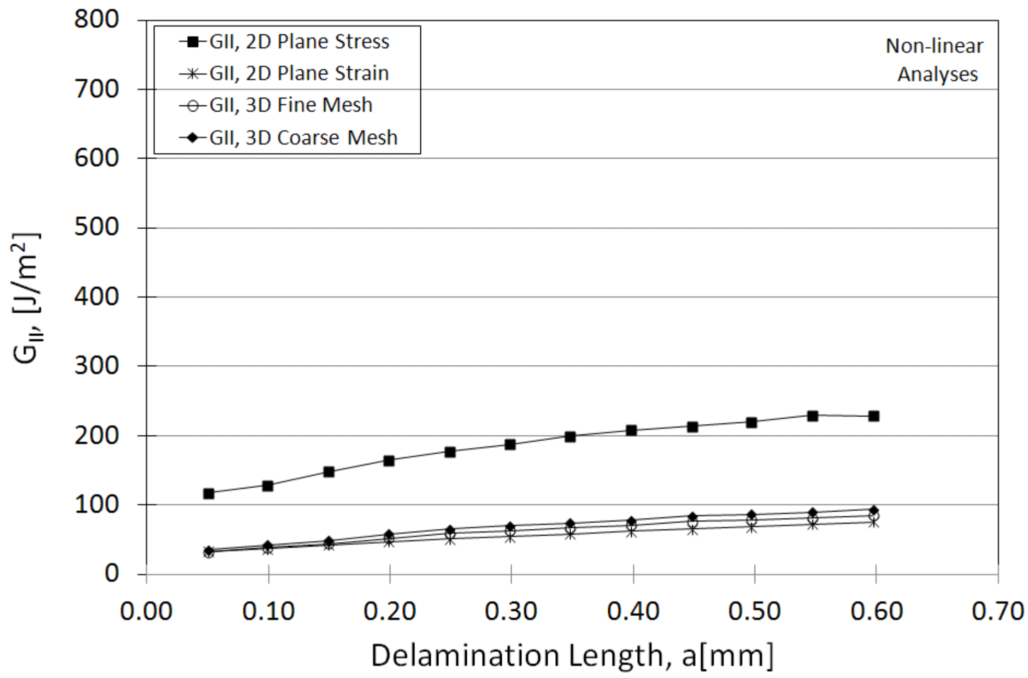

Figure 4-23: Comparison of G_{II} of 2D models and middle section of 3D models

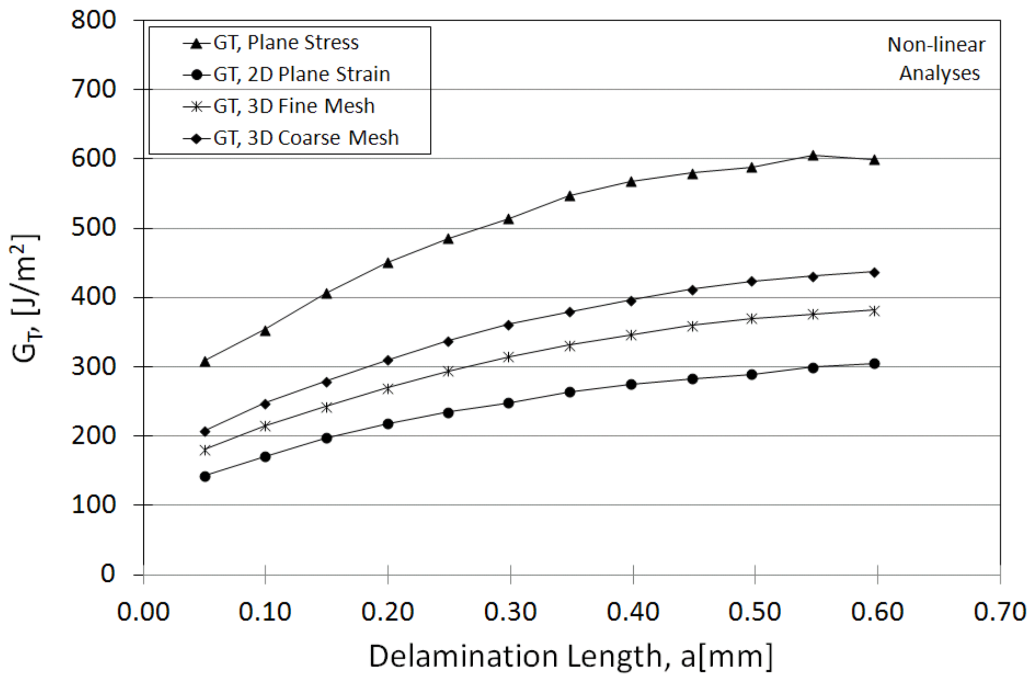

Figure 4-24: Comparison of G_T of 2D models and middle section of 3D models

For the crack opening mode (mode I), the 2D plane stress model estimates the maximum strain energy release rate (G_I), while the 2D plane strain model estimates the minimum. 3D model estimates nearly the average of the 2D plane stress and the 2D plane strain models. It is also noted that the G_I calculated using the coarse mesh 3D model is higher than the fine mesh 3D model. For the sliding shear mode (mode II), the 2D plane stress model estimates the maximum strain energy release rate (G_{II}), and the ones predicted by the 2D plane strain and 3D model estimates are similar. Hence for total strain energy level (G_T), which is the sum of G_I and G_{II} and G_{III}, has the same trend as was observed for G_I. In other words, the 2D plane stress and 2D plane strain models define the envelope for the 3D model, while 2D plane stress estimates are more conservative. These observations are in line with the trends reported for global response analyses. Again, it should be emphasized that for 2D models the G_{III} is equal to zero, and for 3D models at the center of the specimen G_{III} approaches to zero.

Comparison of calculated ratio of the total strain energy release rate (G_T) to the critical fracture toughness (G_c) for 2D plane stress, 2D plane strain and 3D models are presented Figure 4-25. Here the critical fracture toughness is calculated using Equation (3.1) presented in Chapter 3, which is repeated here for completeness:

$$G_c = 75.3 + 214.7\left(\frac{G_S}{G_T}\right) - 70.5\left(\frac{G_S}{G_T}\right)^2 + 327.4\left(\frac{G_S}{G_T}\right)^3 \quad \text{4-1}$$

Note that for calculation of the critical fracture toughness (G_c), the analytically obtained G_I, G_{II} and G_{III} values are used. While this seems contradictory, this is only because G_I, G_{II} and G_{III} appear on the right hand side of the mixed mode equation. It must be noted that the constants that appear in the criterion are fitted using experimental data. Nonetheless, G_I, G_{II} and G_{III} values have to be estimated accurately to obtain a realistic fracture toughness value.

The trend observed in Figure 4-25 is similar to the previous ones. The 2D plane stress and 2D plane strain models define the envelope for the 3D model, while 2D plane stress model estimates are more conservative. It is observed for all the three models the G_T/G_c ratio is above unity indicating potential for delamination growth. As the delamination length increases, the G_T/G_c increases. The G_T/G_c curve flattens approximately when the delamination length equals to 0.6 mm.

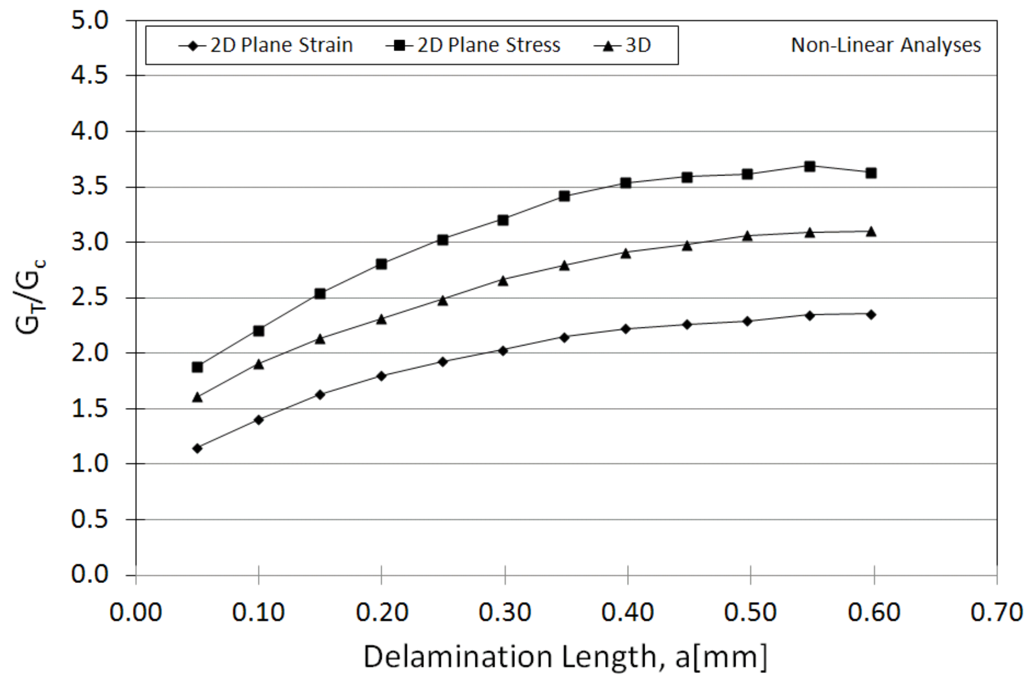

Figure 4-25: Comparison G_T/G_c of 2D models and middle section of 3D model

4.3.2.2 Delamination growth potential in 3D Models

In 2D (plane strain or plane stress) models, the mode III strain energy release rate (G_{III}) is zero, and the shear strain energy release rate (G_s) is equal to the mode II strain energy release rate (G_{II}). Hence forth, the delamination growth potential estimated by 2D model, will only be valid if in reality the mode III strain energy release rate is equal or close to zero.

The ratio of the mode III energy release rate (G_{III}) to the total shear energy release rate (G_s) obtained using the fine mesh 3D model is depicted in Figure 4-26. The variation of G_{III}/G_T through different specimen depths is shown in Figure 4-27. Around the free edges the dominated shear mode is the scissoring mode (G_{III}) while it gradually decreases to zero by moving away from the free edges. For the 2D models, G_{III} is assumed to be zero; hence this assumption is valid if the point of interest is away from the free edges.

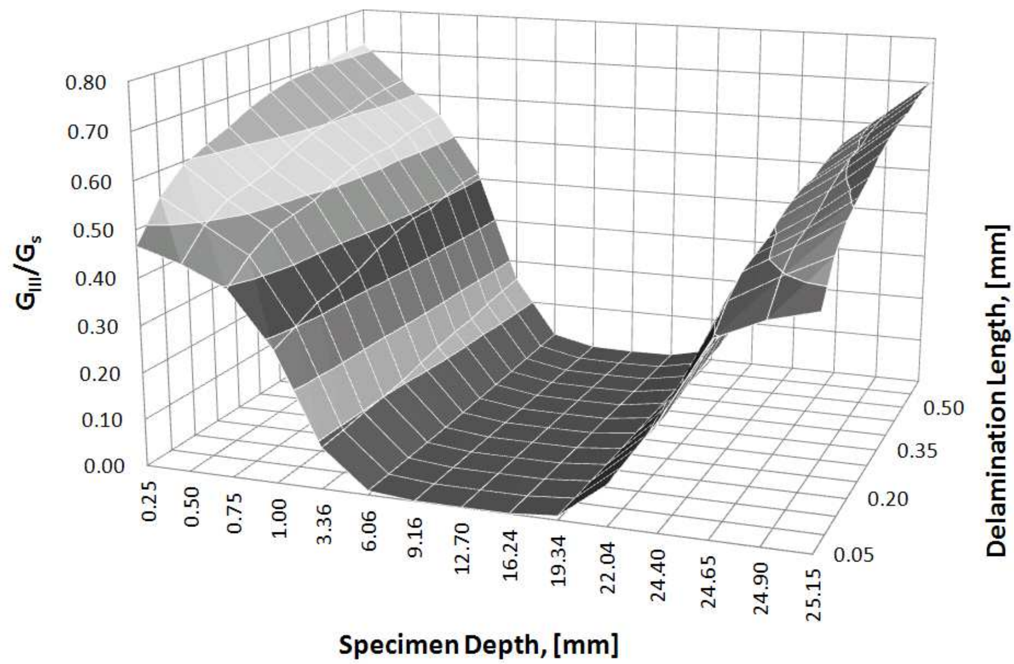

Figure 4-26: G_{III}/G_s ratio for fine mesh 3D model

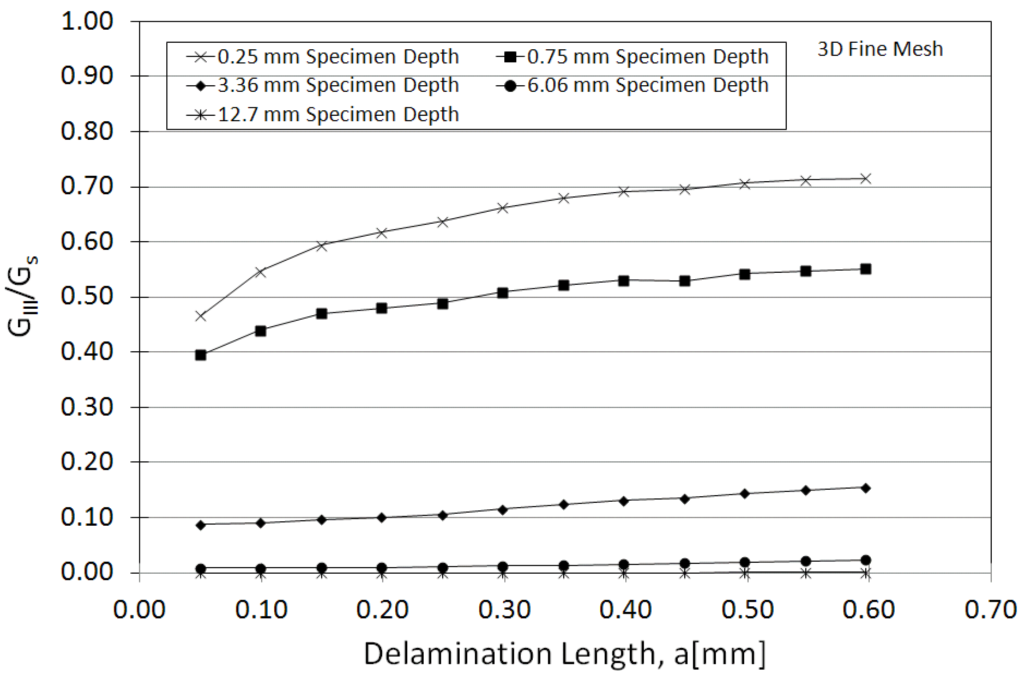

Figure 4-27: G_{III}/G_T at different specimen depths of the fine 3D model

The distribution of mode I strain energy release rate (G_I) and the total strain energy release rate (G_T) is depicted Figure 4-28. The ratio of the total strain energy release rate (G_T) to the critical fracture toughness (G_c) for the fine mesh 3D model is shown in Figure 4-29. Although the total strain energy release rate decreases by moving away from the free edges, the mode I (G_I) energy release rate increases similar to the G_T/G_c ratio, meaning that the mode I is more critical for the delamination to propagate.

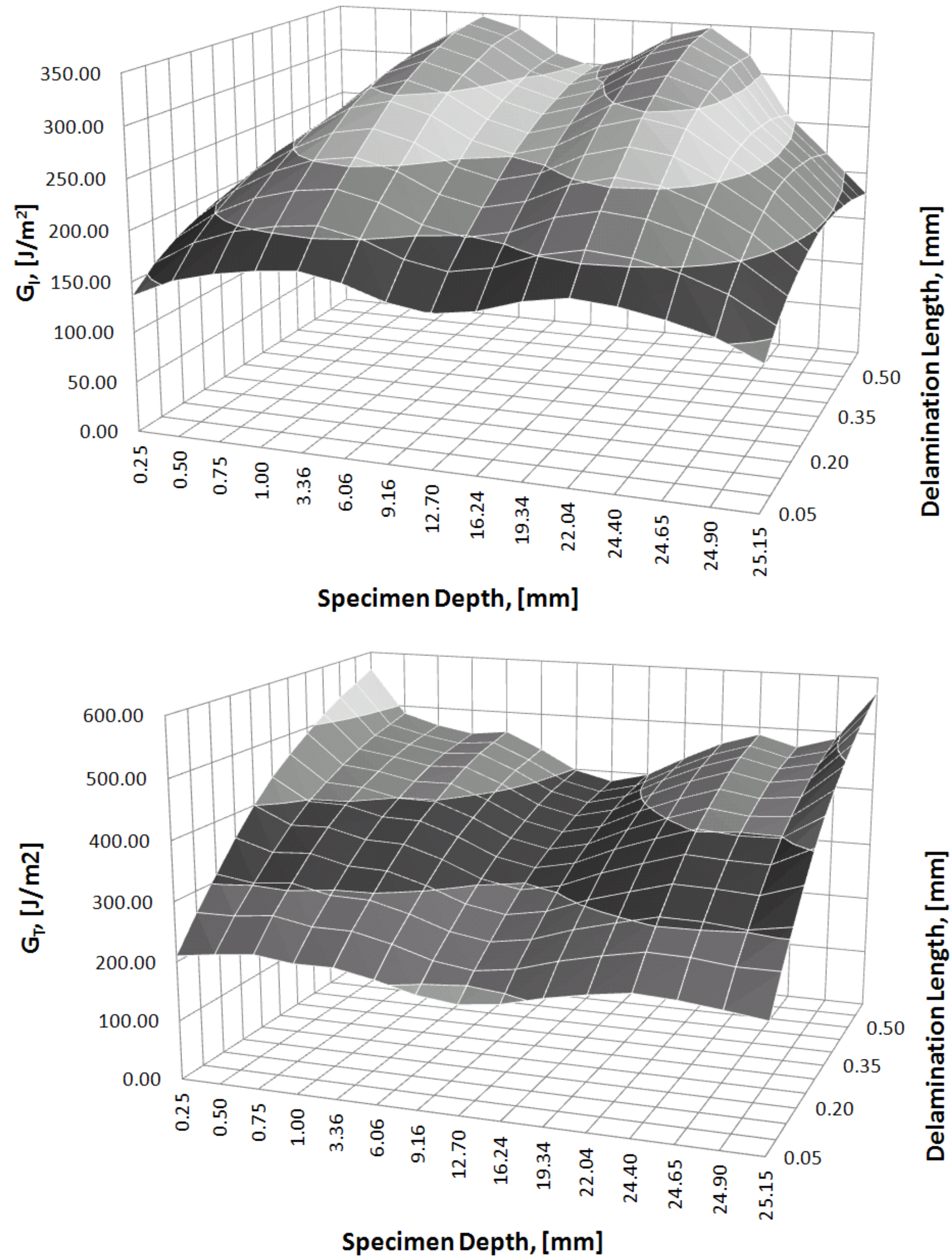

Figure 4-28: Distribution of G_I, G_T for the fine 3D model

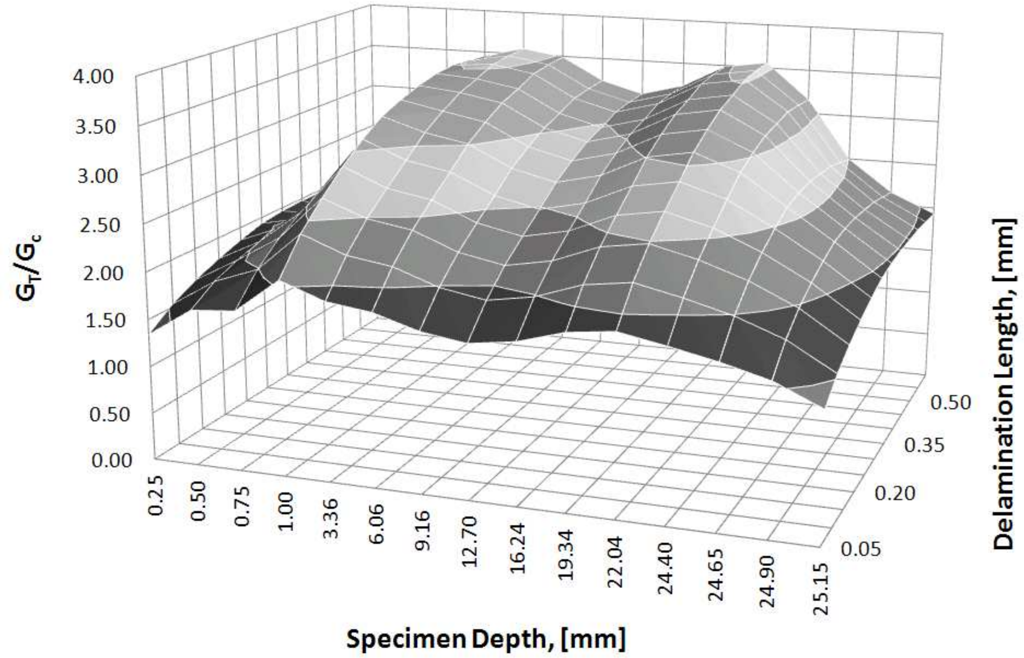

Figure 4-29: Distribution of G_T/G_C for the fine 3D model

4.3.2.3 Effect of Element Order

For the 2D plane strain and 2D plane stress models, both linear (first order) and quadratic (higher order) elements are considered to investigate the effect of element order on the strain energy release rates. The results are compared in Figure 4-30 for 2D plane strain elements, and in Figure 4-31 for 2D plane stress elements. As can be seen from Figure 4-30, estimated strain energy components with the model consisting of first order elements are higher than that of the model with quadratic elements. This result might have been expected in light of the strain data presented in Figure 4-20. For 2D plane strain analyses, with first order elements higher strain values was predicted, which in turn, increases the strain energy release rate. For 2D plane stress model, the results presented in Figure 4-31 indicate that the element order does not have a significant effect on the strain energy release rates. This, again, is in agreement with the strain predictions presented in Figure 4-20.

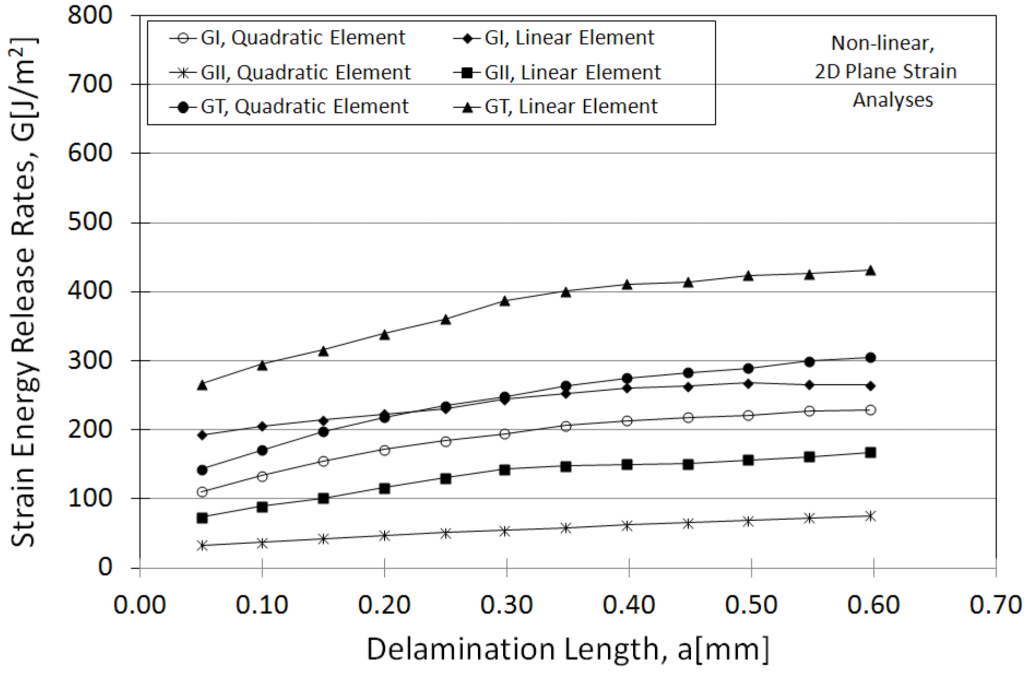

Figure 4-30: Comparison of linear and quadratic reduced integrated elements in 2D plane strain model

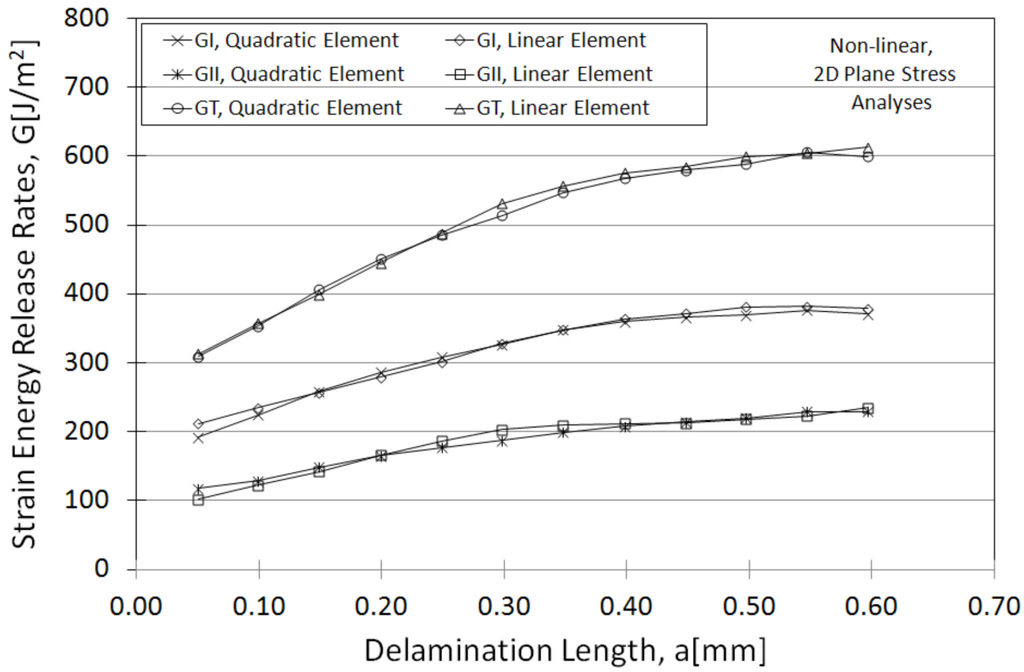

Figure 4-31: Comparison of linear and quadratic reduced integrated elements in 2D plane stress model

4.3.2.4 Effect of Constraints at Crack Front

The effect of different constraints at the crack front is investigated. Two types of analyses are conducted. In the first one, the "TIE MPC" option available in the Abaqus/Standard element library is used to constrain all the translational and rotational degrees of freedoms at the crack tip (total 6 degrees of freedom). In the second one, "LINK MPC" option available in the Abaqus/Standard element library is used to constrain only the translational degrees of freedoms (total 3). The comparison of the results obtained using these two different constraint types for non-linear plane strain analyses is presented in Figure 4-32. As could be seen from this figure, in addition to constraining the translational degrees of freedom, constraining the rotational degrees of freedom does not have a significant effect on the calculated strain energy release rates The same analyses is repeated for non-linear plane stress analyses, and the same results are obtained. It must be noted, the effect of different constrains at the crack front is only a concern for 2D analyses and not for 3D analyses, since the 3D elements have no rotational degrees of freedoms at their nodes.

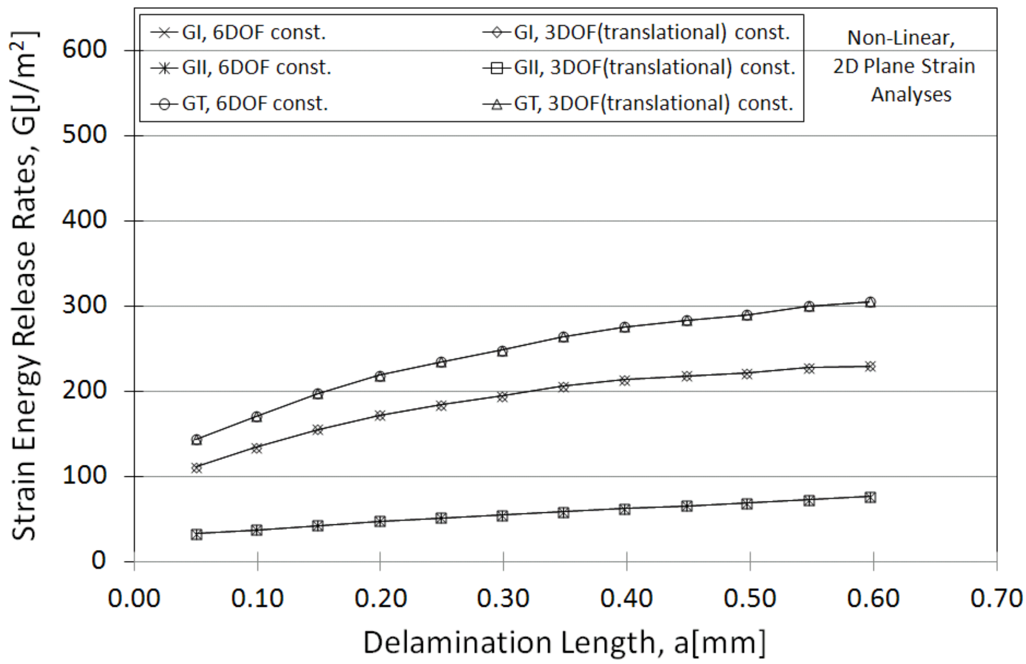

Figure 4-32: Effect of constraints at crack front

4.3.2.5 Effect of Geometric Nonlinearity

In the global response section, it was shown that geometric linear analyses yields unrealistic bending effects, hence geometric nonlinear analyses should be preferred to eliminate these effects. However geometric linear analyses was conducted for 2D plane strain model and presented here for completeness. The comparison of strain energy release rates for 2D plane strain analyses with quadratic elements is depicted in Figure 4-33.

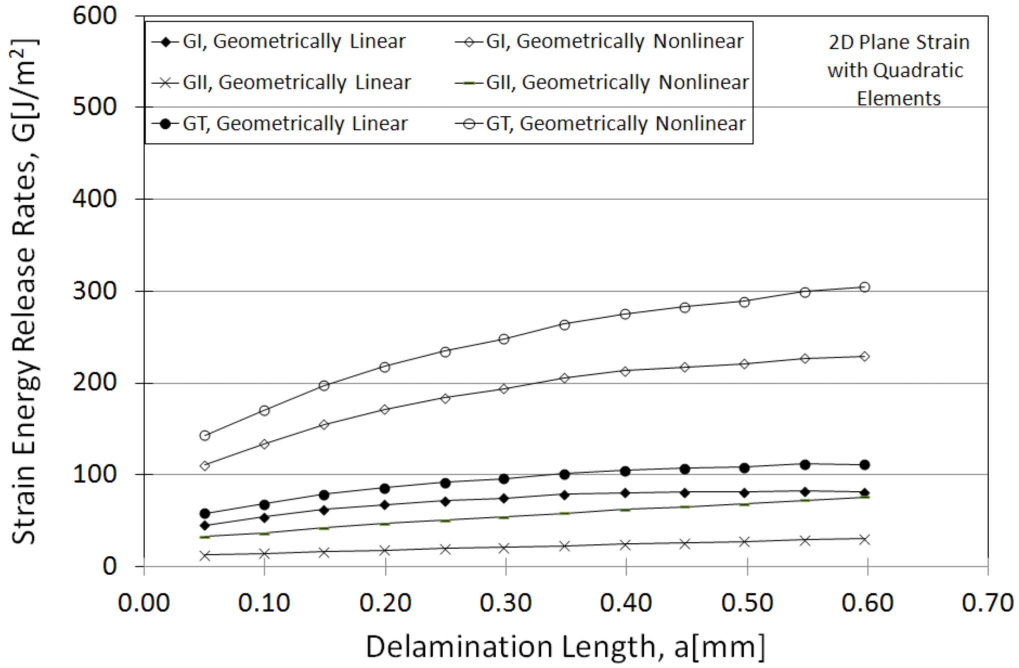

Figure 4-33: Effect of geometric nonlinearity

4.3.2.6 Effect of Mesh Density near Free Ends

In order to investigate the effect of mesh density near free ends, on the strain energy release rates, two 3D models whose details are described in Section 4.2 are prepared. The model with fine mesh has a high mesh density near the free edges; on contrary the model with coarse mesh has uniform mesh distribution. The calculated strain energy release rates for fine and coarse 3D models are depicted in Figure 4-34 and Figure 4-35 respectively. In order to compare the total strain energy release rates of the two models more easily, the variation of G_T through the specimen depth, for a fixed delamination length of 0.6 mm is presented in Figure 4-36.

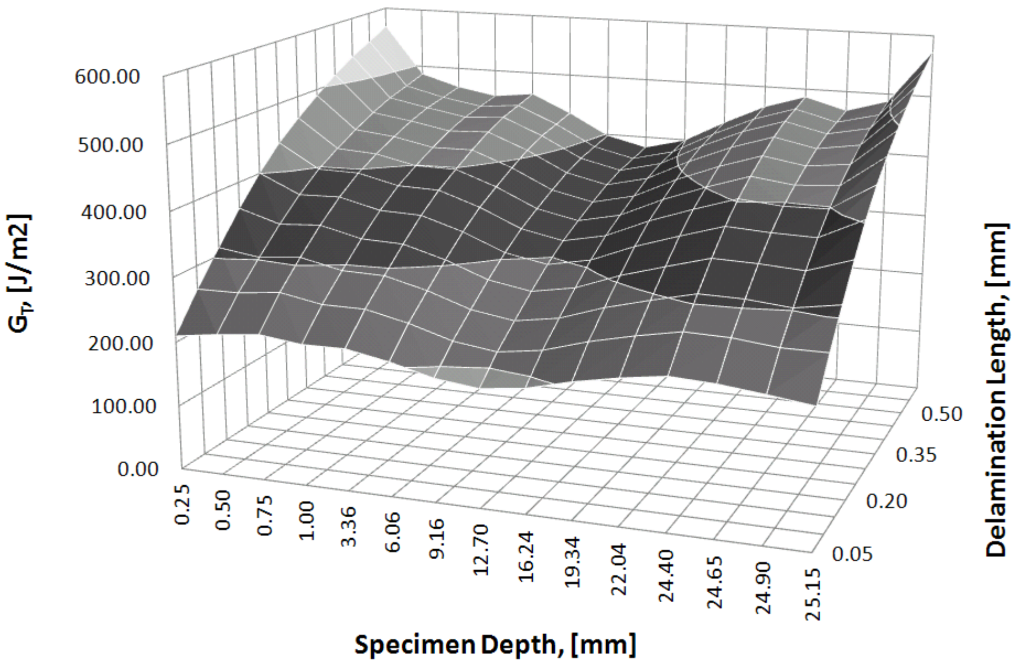

Figure 4-34: Total strain energy release rate (G_T) for the fine 3D model

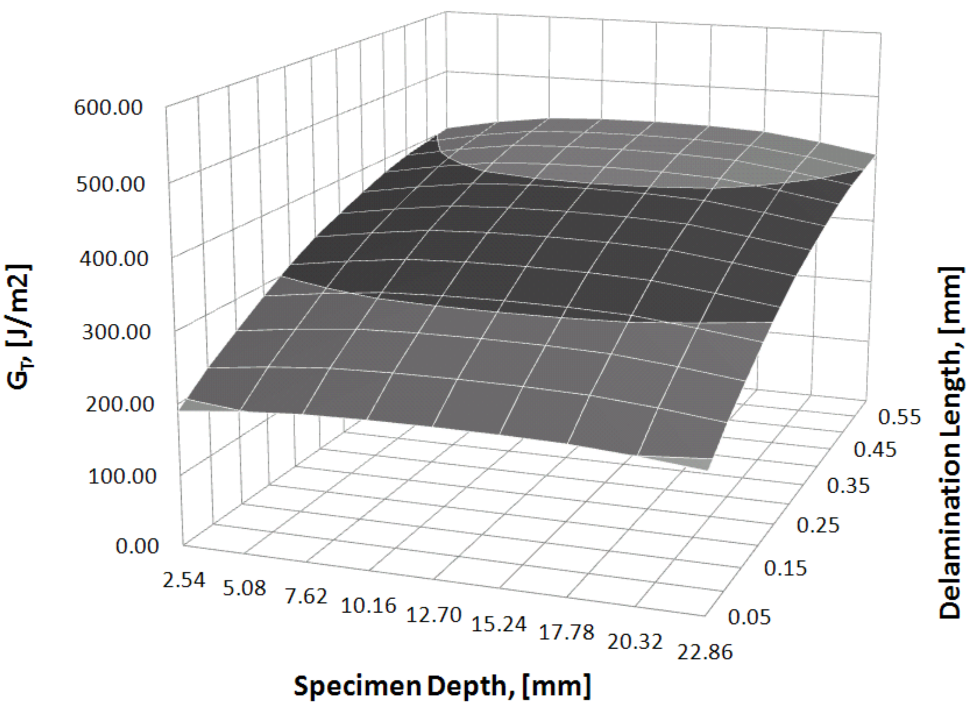

Figure 4-35: Total strain energy release rate (G_T) for the coarse 3D model

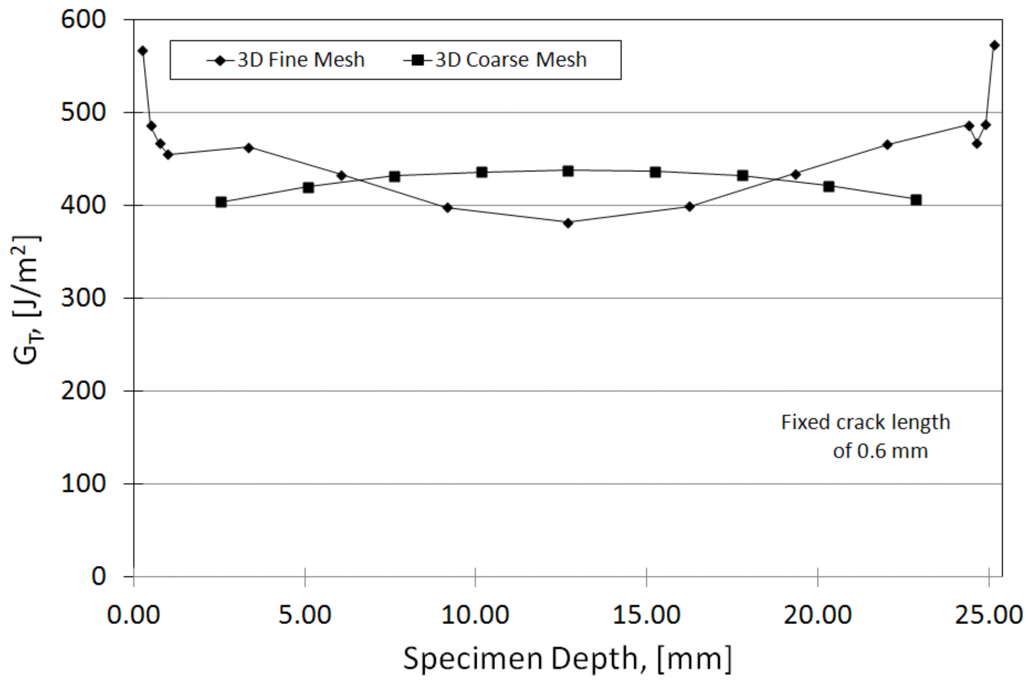

Figure 4-36: Comparison of G_T for fixed delimination length of 0.6 mm

As could be seen from Figure 4-34, Figure 4-35 and Figure 4-36, the total strain energy release rate is not constant through the specimen depth. For the fine mesh analyses, a considerable increase in the strain energy release rate is observed close to the edges, which could not be captured by the coarse mesh analyses. From Figure 4-36 it can also be observed that with the fine mesh the minimum strain energy release is predicted at the center of the specimen. However, the same figure shows that the coarse mesh model predicts the maximum strain energy release at the center of the specimen, and the minimum strain energy release at the free edges.

The comparison of the shear strain energy rate (G_s) to the total strain energy level (G_T) ratio calculated using fine mesh and coarse mesh 3D models are shown in Figure 4-37 and Figure 4-38. The shear strain energy rate (G_s) is the sum of mode II (G_{II}) and mode III (G_{III}) strain energy rates. For a fixed delamination length of 0.6 mm, the variation of G_s/G_T through specimen depth is presented in Figure 4-39. Similar to the total strain energy rate, investigation of Figure 4-39 shows that the G_s/G_T ratio is not constant through the depth of the specimen. At the center of the specimen, both models produce a similar G_s/G_T ratio, but close to the edges, the coarse model cannot predict the increase in the G_s/G_T ratio. The model with fine mesh estimates a maximum G_s/G_T ratio around 0.7, while the other model estimates a maximum of around 0.3. Hence, it can be concluded the mesh density in the coarse model is not satisfactory to track the shear energies around the free edges.

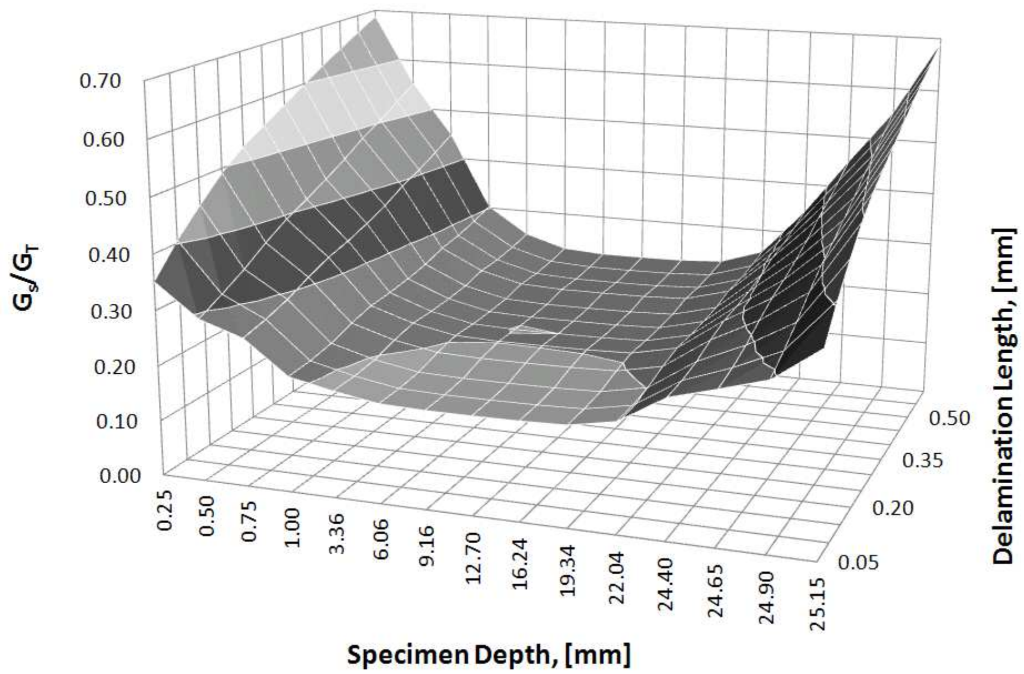

Figure 4-37: G_s/G_T of fine 3D mesh

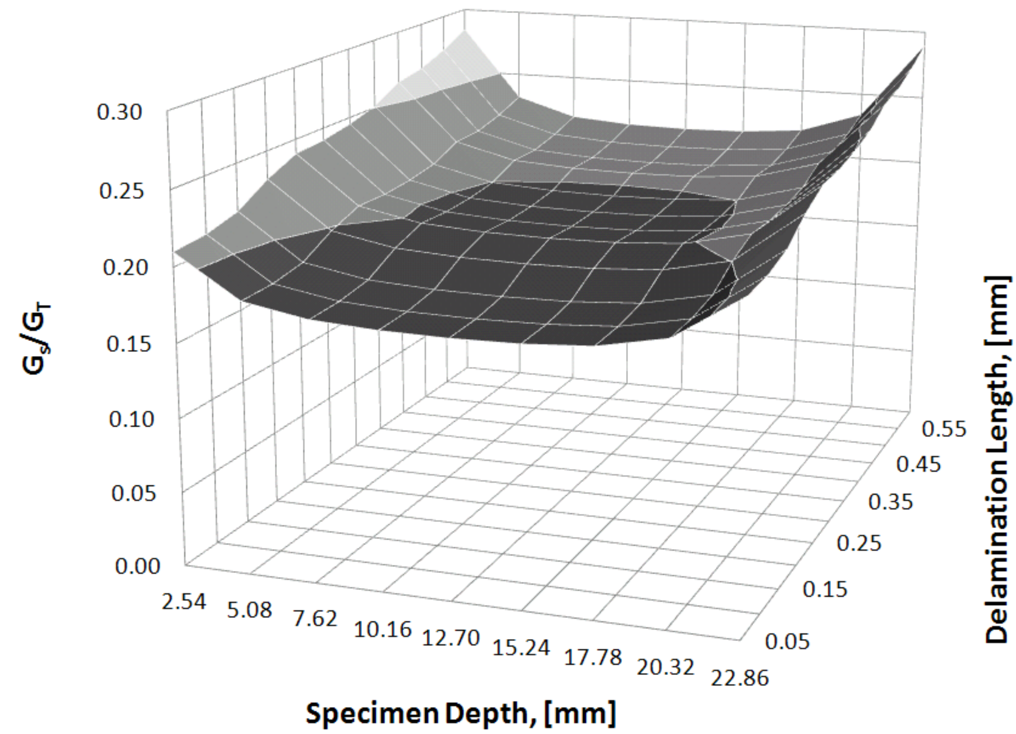

Figure 4-38: G_s/G_T of coarse 3D mesh

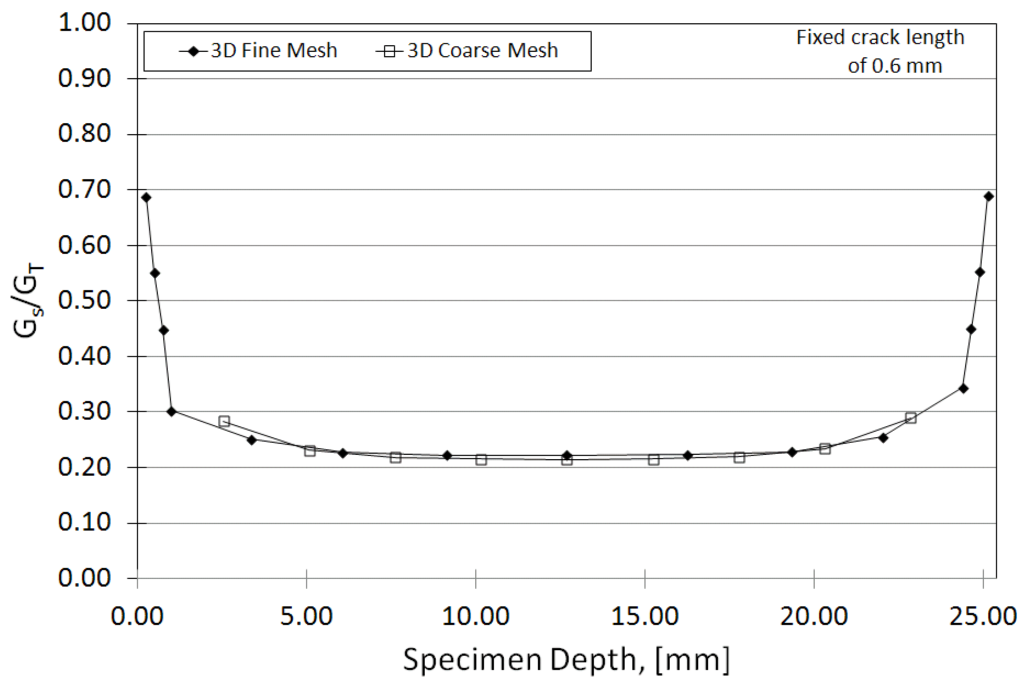

Figure 4-39: Comparison of G_s/G_T for fixed delimination length of 0.6 mm

4.4 Effect of Initial Defect Location on Delamination Growth Potential

Due to manufacturing, assembly or in service problems, (initial) defects may occur which may reduce the resistance of the structure to the design loads. During manufacturing a process error or a material problem may lead to some initial delaminations, porosities or resin rich regions. In montage assembly, a drop of a tool to the structure or un-intendaly crash of the structure may lead impact damages as fiber breakages or delaminations. While in service use, run-away debrises or environmental issues may cause delaminations. Hence in most situations the design should account for these flaws which are named the damage tolerant design. From a design point of view the following question arises: “Does the location of a particular (initial) defect or flaw effect the potential of delamination growth or crack propagation?” In other words, for example, does an (initial) defect or flaw that might have occurred at the free edge has the same detrimental effect as the one that might have occurred at the center of the assembly. Due to these facts, the effect of (initial) defect or flaw location is investigated by using the 3D finite element models. Particularly, two cases are studied; the effect of a (initial) defect or flaw that might have occurred at the free edge, and the one that might have occurred at the center of the assembly. This is done by embedding some initial defects into the 3D finite element mode I and comparing the delamination growth potentials. Both fine and coarse mesh finite element models are considered to study the effect of different modeling techniques.

4.4.1 Description of the Problem

The skin-stiffener assembly described in Chapter 3 is considered to investigate the effect of initial defect location on the delamination growth potential. Two individual cases are considered. The first defect, called "Defect 1" hereinafter, is located near the free edge, and the second defect, called "Defect 2" hereinafter, is located in the middle of the specimen. The 3D finite element models with coarse and fines meshed that have been evaluated in Chapter 4 have been used to investigate the effect of mesh sensitivity. In the fine 3D model the defects are around 6 mm x 1 mm, while in the coarse model the defects are around 0.75 mm x 1 mm. The locations of the defects are depicted in Figure 4-40. In summary two different initial defect locations have been studied using two different analyses techniques.

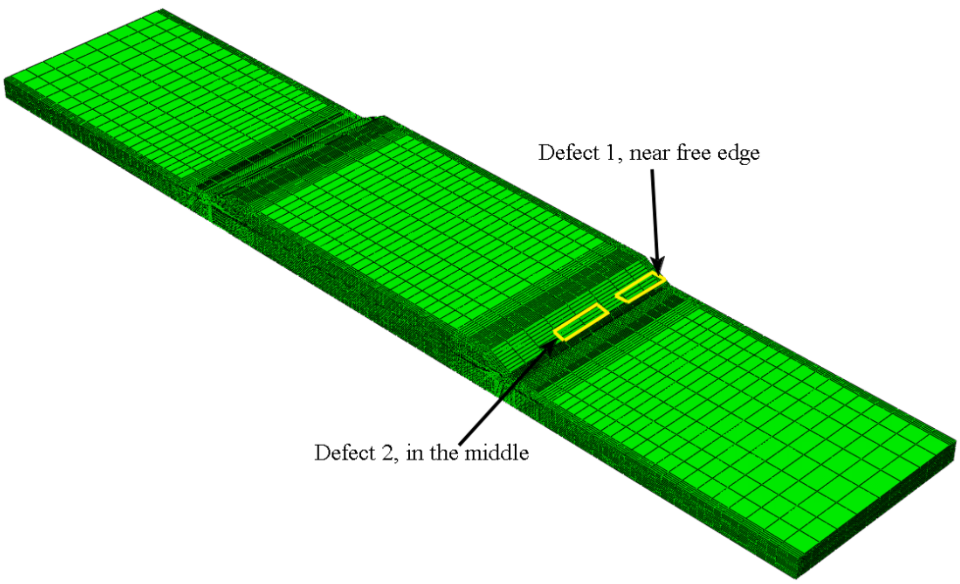

Figure 4-40: Defects in the fine 3D models

4.4.2 Results

The deformed shapes are depicted for defect 1 and defect 2 of the fine 3D model in Figure 4-41 and Figure 4-42 respectively.

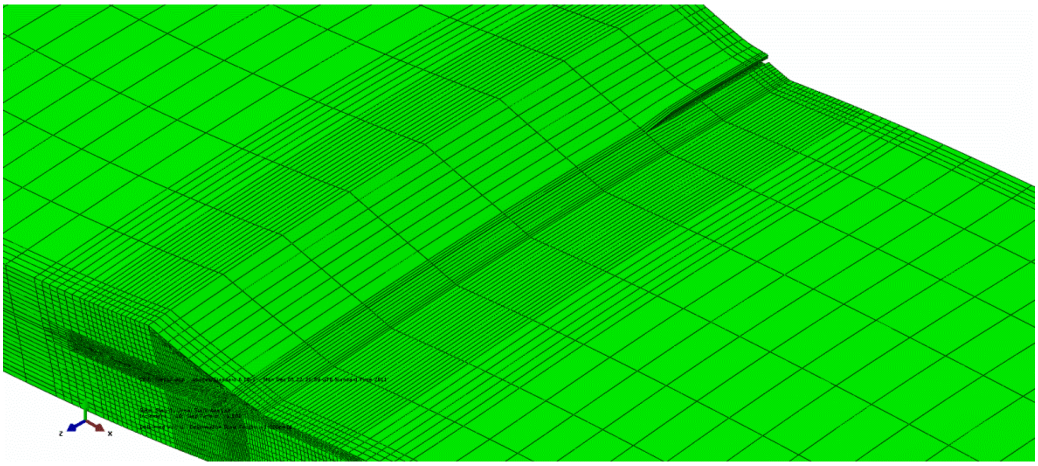

Figure 4-41: Deformation shape of defect 1 in fine 3D model

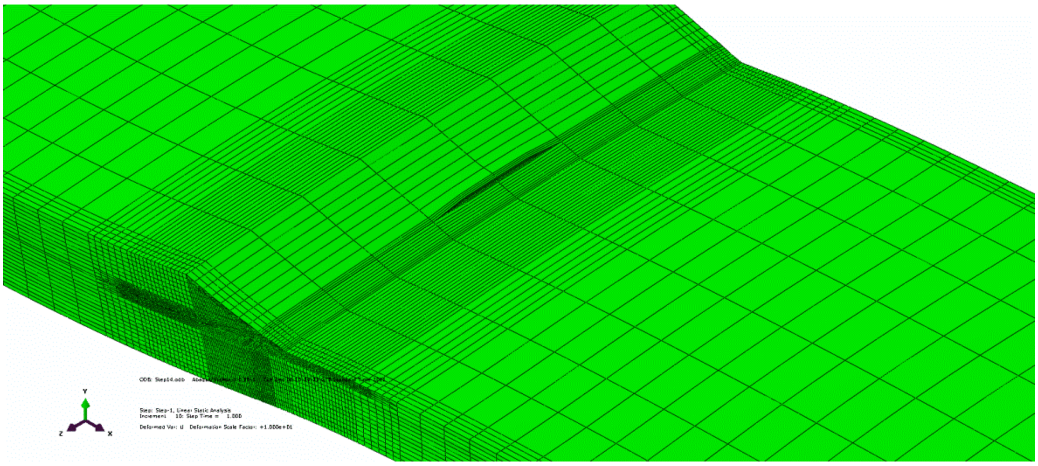

Figure 4-42: Deformation shape of defect 2 in fine 3D model

For all the analyses conducted, the total strain energy release rates, the calculated critical fracture toughness values, and the ratio of the total energy to the fracture toughness are tabulated in Table 4-1. The data presented in Table 4-1 is extracted at the center of the defect.

Table 4-1: Total strain energy comparison of the defects

		G_T [J/m^2]	G_c [J/m^2]	G_T/G_c
Fine 3D model	Defect 1, Near free edge	463	140	3.37
	Defect 2, In the middle	371	127	2.93
Coarse 3D model	Defect 1, Near free edge	409	131	3.13
	Defect 2, In the middle	419	128	3.28

As could be seen from Table 4-1, in the fine mesh 3D model, the defect near the free edge gives a higher G_T/G_c compared to the defect in the middle. This indicates that in a component subjected to pure axial loading, having a defect (or flaw) near the free edge of the component is more critical compared to a defect of similar size in the middle of the component. It should be noted that in a 'damage tolerant design' approach, based on a reduced allowable stress was used, this difference couldn't be distinguished. In other words, in a 'damage tolerant design' approach, the flaws at the free edge and the center of the component would have been treated the same, which based on the data presented in Table 4-1 should not be.

On the other hand, for the coarse mesh 3D model, the results presented in Table 4-1 indicate that the initial flaw in the middle of the specimen is more critical than the one near the free edge. This observation is the complete opposite as the one made using the fine mesh 3D model. For the defect at the middle of the specimen, the coarse and the fine mesh models predict similar G_c

values. This is rather expected since G_c is based on G_s/G_T ratio (see equation (4-1)), and as demonstrated in Figure 4-39 both the fine and coarse mesh 3D models predict very close G_s/G_T values at the center of the specimen. However, as discussed before the coarse mesh cannot accurately track the strain energy release rates near the free edges. Henceforth, the results by the coarse mesh 3D are misleading, and care must be taken in creating the mesh near the free edges.

CHAPTER 5

SUMMARY, CONCLUSIONS AND FUTURE WORKS

5.1 Summary

The objective of this study was to investigate the debonding/delamination onset and growth potential in a bonded fiber reinforced composite skin-flange assembly using the virtual crack closure technique (VCCT). The effect of different modeling techniques was investigated including element type, element order, mesh density, and geometric non-linearity parameters. Finally, effect of initial defect location on delamination growth potential was investigated.

In the first section of this study, the effect of different parameters on the global response was investigated. During the course of the work, 2D plane stress, 2D plane strain, and 3D models of an undamaged specimen were compared with the experimental data. Both geometric linear and non-linear finite element analyses were conducted to understand the effect of geometric non-linearity. Models with linear and quadratic elements were analyzed to investigate the contribution of element order on the global response results. For the 3D models, mesh density parameter was investigated by analyzing a coarse mesh 3D model and a fine mesh 3D model, which had a fine mesh near the free edges of the specimen.

In the second section of this study, after having a sound understanding of the parameters on the global response, debonds of different lengths were introduced to the finite element models to investigate the potential of delamination growth using a fracture mechanics based approach (VCCT).

In the third and final section of this study, effect of initial defect location on delamination growth potential was investigated. Initial defects were embedded to the fine and coarse mesh 3D models to investigate the capability of mesh density. In addition similar defects were embedded to the 3D models at different locations (i.e.: close to the free edge, far away from the free edge) in order to understand the effect of damage location on the potential of delamination growth.

5.2 Conclusion

Comparison of the finite element results with the experimental ones showed that for the global response of the bonded skin-flange assembly under tension loading:

- The 2D plane strain and 2D plane stress models form the upper and lower bound, while the analyses with the 3D model resulted in excellent agreement with the experimental data. This is confirmed both using the global force-deformation data, and the strain data extracted from the middle of the flange. Generally, the 2D plane strain model yields a stiffer response, and the 2D plane stress model results in a more flexible response. If only the global response of the specimen is under consideration, 2D plain strain and plane stress analyses can be conducted with great accuracy.

- For the 3D model, no significant difference is observed between the fine mesh and coarse mesh models.

- During the tensile tests, due to the large deformations, a shift in the neutral axis of the specimen causes an eccentric loading. Hence, although pure tensile loads are applied, bending of the specimen is observed from the experimental strain data. A comparison of the strain data at the flange has shown the importance of conducting geometrically non-linear analyses. The comparison conducted at the flange of the specimen shows that the strain values obtained are unrealistic for linear analyses. This is due to the fact that an excessive and unrealistic bending is observed in linear analysis, such that the normal strain caused by axial loading are eliminated by the normal strains caused by the excessive bending of the specimen.

- It has been observed that for the 2D plane strain and plane stress analyses; the force-deformation response of the specimen is not affected by the element order (linear versus quadratic). However, some differences are observed for strain output at the middle of the flange. For VCCT analyses higher order elements are recommended, since the strain energy release rate is a function of the deformations at the crack tip, which is a function of the strain.

A parametric virtual crack closure analyses is conducted and the following observations are made:

- For the total strain energy release rate (G_T), it is observed that the 2D plane stress and 2D plane strain models define the envelope for the 3D model. The total energy estimates obtained from the 2D plane stress estimates are more conservative. This observation is in line with the trends for the global response analyses. The total strain energy release rate to the fracture toughness ratio (G_T/G_c) comparison complies with this observation as well; where the 2D plane stress and 2D plane strain models define the envelope for the 3D model, while 2D plane stress model estimates are more conservative.

- With 2D plane strain and plane stress analyses the mode III strain energy release rate (G_{III}) cannot be estimated. In other words, for 2D analyses G_{III} is equal to zero. The 3D analyses conducted have shown that for the skin-flange assembly under consideration, the dominant shear mode around the free edges is the scissoring mode (G_{III}). The 3D analyses indicate that the G_{III} gradually decreases to zero away from the free edges. Hence, the delamination growth potential estimated by 2D models will only be valid if in reality the mode III strain energy release rate is equal or close to zero, which is valid if the point of interest is sufficiently away from the free edges.

- For 3D analyses it is observed that mesh density has a significant effect on the strain energy release rates near the free edges. In order to capture the real behavior of the specimen, fine mesh should be used near the free edges. Coarse mesh around the free edges has a potential risk of missing the tendency of rapid increase of shear strain energy release rate (G_s).

- The results obtained in this study indicate that in a component subjected to pure axial loading, having a defect (or flaw) near the free edge of the component is more critical compared to a defect of similar size in the middle of the component. However, the analyses results also indicate that the coarse mesh 3D models cannot accurately track the strain energy release rates near the free edges. Henceforth, the results by the coarse mesh 3D could be misleading, and care must be taken in defining the satisfactory mesh density near the free edges.

In summary, if only the global response is under consideration, both 3D fine and coarse mesh models comply with the experimental results, and the 2D plane strain and plane stress analyses provide satisfactory results (the 2D plane strain forms the upper bound and 2D plane stress forms the lower bound). However, care must be taken in delamination onset analysis. In order to capture a more realistic behavior, 3D analyses with a satisfactory mesh density should be used near the free edges. It should be noted that from a computation time perspective, 3D mesh models have very long computation times compared to 2D models. The fine mesh 3D model, which is only fine near the free edges, spends nearly six times more computation time compared to the coarse mesh 3D model. Therefore, it is critical to define the area of interest and decide on the required mesh density or modeling technique before conducting a delamination onset analyses.

5.3 Future Work and Recommendations

During the course of the work, test data obtained from the literature was used. For future studies, more controlled and rigorous testing is recommended. Results of this study show that, while a certain modeling technique yields satisfactory results for the global response, it cannot capture the strain energy release rate. It is crucial that the finite element analyses are validated against experimental data.

During the course of work, pure axial loading is investigated. Investigation of different load cases is crucial. The results obtained from this study may not be applicable to a skin-flange assembly under pure bending.

The results obtained in this study show that 3D finite element analysis, which is the most expensive from a computational point of view, produces the most accurate results. To shorten the computation times, and to avoid the usage of 3D modeling technique in complex problems, hybrid modeling techniques (2D/3D hybrid) should be further investigated.

REFERENCES

[1] Abaqus ® 6.10, *Abaqus/CAE Users Manual, 2010*

[2] Alfano G., Crisfield M.A., *Finite Element Interface Models for the Delamination Analysis of Laminated Composites: Mechanical and Computational Issues*, International Journal for Numerical Methods in Engineering, 50(7): 1701-1736, 2001

[3] ASTM Standard D5528, 01(2007)e3, *Standard Test Method for Mode I Interlaminar Fracture Toughness of Unidirectional Fiber Reinforced Polymer Matrix Composites*, ASTM International, 2007

[4] Benzeggagh, M.L., Kenane, M., *Measurement of Mixed-Mode Delamination Fracture Toughness of Unidirectional Glass/Epoxy Composites with Mixed-Mode Bending Apparatus*, Composites Science and Technology, 56(4): 439-449, 1996

[5] Bonhomme J., Argüelles A., Castrillo M.A., Vina J., *Computational Models for Mode I Composite Fracture Failure: the Virtual Crack Closure Technique versus the Two-Step Extension Method*, Meccanica, 45(3): 297-304, 2009

[6] Camanho P.P., Davila C.G., Ambur D.R., *Numerical Simulation of Delamination Growth in Composite Materials*, NASA Langley Research Center, NASA/TP-2001-211041, 2001

[7] Camanho P.P., Davila C.G., *Mixed-Mode Decohesion Finite Elements for the Simulation of Delamination in Composite Materials*, NASA Langley Research Center, NASA/TM-2002-211737, 2002

[8] Campbell F.C., *Manufacturing Processes for Advanced Composites*, Elsevier Ltd., 2004

[9] Descartes R., *La Géométrie* (The *Geometry*), 1637

[10] Gillespie Jr., J.W., Carlsson, L.A., Pipes, R.B., Rothschilds, R., Trethewey, B., Smiley, A., *Delamination Growth in Composite Materials*, NASA CR 176416, 1985

[11] Hansen P., Martin R., *DCB, 4ENF and MMB Delamination Characterisation of S2/8552 and IM7/8552*, European Research Office of the U.S. Army, 1999

[12] Heslehurst RB, *Design and Analysis of Composite Structural Joints*, Abaris Training, 2008

[13] Jimenez M.A., Miravete A., *Application of the Finite Element Method to Predict the Onset of Delamination Growth*, Journal of Composite Materials, 38 (15): 1309-1335, 2004

[14] Johnson W.S., Butkus L.M., Valentin R.V., *Applications of Fracture Mechanics to the Durability of Bonded Composite Joints*, U.S. Department of Transportation, Federal Aviation Administration, 1998

[15] Kageyama K., Kikuchi, M., and Yanagisawa, N., *Stabilized End Notched Flexure Test: Characterization of Mode II Interlaminar Crack Growth*, Composite Materials: Fatigue and Fracture, Third Volume, ASTM STP 1110, 1991, pp. 210-225.

[16] Kohnle C., Mintchev O., Schmauder S., *Elastic and Plastic Fracture Energies of Metal/Ceramic Joints*, Computational Material Science, 25: 272-277, 2002

[17] Krueger R, *The Virtual Crack Closure Technique: History, Approach and Applications*, NACA/CR-2002-211628, ICASE Report No. 2002-10, 2002

[18] Krueger R., Paris I.L., O'Brien T.K., Minguet P.J., *Fatigue Life Methodology for Bonded Composite Skin/Stringer Configurations*, NASA/TM-2001-210842, ARL-TR-2432, 2001

[19] Krueger R., Cvitkovich M.K., *Testing and Analysis of Composite Skin/Stringer Debonding Under Multi-Axial Loading*, NASA/TM-1999-209097, ARL-MR-439, 1999

[20] Krueger R., *Three Dimensional Finite Element Analysis of Multidirectional Composite DCB, SLB and ENF Specimens*, ISD-Report No. 94/2, 1994

[21] Krueger R., König M., Schneider T., *Computation of local energy release rates along straight and curved delamination fronts of uni-directionally laminated DCB- and ENF-specimens*, in Proceedings of the 34th AIAA/ASME/ASCE/AHS/ASC SSDM Conference, 1993

[22] Li J., Lee S.M., Lee E.W., O'Brien T. K., *Evaluation of the edge crack torsion (ECT) Test for mode III interlaminar fracture toughness of laminated composites*, Journal of Composites Technology and Research, 19(3): 174-183, 1997

[23] MIL-HDBK-17-1E Volume 1, *Polymer Matrix Composite, Guidelines for Characterization of Structural Materials*, 1997

[24] Miracle D.B., Donaldson S.L., *ASM Handbook Volume 21: Composites,* ASM International, 2001

[25] Niu M.C.Y., *Airframe Structural Design: Practical Design Information and Data on Aircraft Structures,* Adaso Adastra Engineering Center, 2nd Edition, 2006

[26] O'Brien T.K., *Composite Interlaminar Shear Fracture Toughness,* G_{IIc}*: Shear Measurement or Shear Myth?,* Composite Materials: Fatigue and Fracture, Seventh Volume, ASTM STP 1330, pp. 3-18, 1998

[27] O'Brien T.K., *Interlaminar Fracture Toughness: the Long and Winding Road to Standardization*, Composites Part B, 29: 57-62, 1998

[28] Pagano N.J., Schoepner G.A., *Delamination of Polymer Matrix Composites: Problems and Assessment*, Comprehensive Composite Materials, 2: 433-528, 2000

[29] Raju I.S., *Calculation Of Strain-Energy Release Rates With Higher Order And Singular Finite Elements*, Eng. Fracture Mech., 28: 251-274, 1987

[30] Reeder J.R., *A Bilinear Failure Criterion for Mixed-Mode Delamination,* Composite Materials: Testing and Design, Vol. 11, ASTM STP 1206, 1993

[31] Reeder J.R., *3D Mixed-Mode Delamination Fracture Criteria- An Experimentalist's Perspective*, NASA Langley Research Center, 2004

[32] Tvergaard V., Hutchinson J.W., *The Relation Between Crack Growth Resistance and Fracture Process Parameters in Elastic-Plastic Solids,* Journal of the Mechanics and Physics of Solids 40: 1377-1397, 1992

[33] Whitcomb J.D., *Parametric Study of Instability-Related Delamination Growth,* Composite Science and Technology, 25(1): 19-48, 1986

[34] Whitcomb J.D., Raju I.S., *Analysis of Interlaminar Stresses in Thick Composite Laminates With and Without Edge Delamination*, NASA-TM-85738, 1984

[35] Wei Y., Hutchinson J.W., *Interface Strength, Work of Adhesion and Plasticity in the Peel Test,* International Journal of Fracture, 93: 315-333, 1998

[36] Wu E., Reuter Jr. R.C., *Crack Extension in Fiberglass Reinforced Plastics,* T and M report No. 275, University of Illinois, USA, 1965

[37] Yarrington P.W., Collier C.S., *Failure Analysis of Adhesively Bonded Composite Joints via the Virtual Crack Closure Technique*, in Proceedings of the 47th AIAA/ASME/ASCE/AHS/ASC SSDM Conference, 2006